Moment Tensors of Ring-Faulting at Active Volcanoes: Insights into Vertical-CLVD Earthquakes at the Sierra Negra Caldera, Galápagos Islands

Osamu Sandanbata[1,2], Hiroo Kanamori[3], Luis Rivera[4], Zhongwen Zhan[3], Shingo Watada[1], and Kenji Satake[1]

[1]Earthquake Research Institute, the University of Tokyo, Tokyo, Japan.

[2]*Now at* National Research Institute for Earth Science and Disaster Prevention, Ibaraki, Japan.

[3]Seismological Laboratory, California Institute of Technology, Pasadena, CA, USA.

[4]Université de Strasbourg, CNRS, ITES UMR 7063, Strasbourg F-67084, France.

Corresponding author: Osamu Sandanbata (osm3@bosai.go.jp)

Full postal address: 3-1, Tennodai, Tsukuba, Ibaraki, 305-0006, Japan

ORCID: 0000-0002-2361-8482

Key points:

- Dip slip along curved ring faults at volcanoes generate $M_w > 5$ earthquakes dominated by a compensated-linear-vector-dipole component.
- We propose a method for estimating ring-fault parameters by moment tensor inversion using long-period seismic data.

- Our estimation of ring-fault parameters of an earthquake at the Sierra Negra caldera yields results consistent with geodetic observations.

Abstract

Large earthquakes (M_w > 5) with moment tensors (MTs) dominated by a vertical compensated-linear-vector-dipole (vertical-CLVD) component are often generated by dip slip along a curved ring-fault system at active volcanoes. However, relating their MTs to ring-fault parameters has proved difficult. The objective of this study is to find a robust way of estimating ring-fault parameters based on their MT solutions obtained from long-period seismic records. We first model the MTs of idealized ring-faulting and show that an MT component representing the vertical dip-slip mechanism is indeterminate from long-period seismic waves owing to a shallow source depth, whereas the other MT components representing the vertical-CLVD and vertical strike-slip mechanisms are resolvable. We then propose a new method for estimating the arc angle and orientation of ring-faulting using the two resolvable MT components. For validation, we study a vertical-CLVD earthquake that occurred during the 2005 volcanic activity at the Sierra Negra caldera, Galápagos Islands. The resolvable MT components are stably determined from long-period seismic waves, and our estimation of the ring-fault parameters is consistent with the ring-fault geometry identified by previous geodetic studies and field surveys. We also estimate ring-fault parameters of two earthquakes that took place during the 2018 activity at the caldera, revealing significant differences between the two earthquakes in terms of slip direction and location. These results show the usefulness of our method for estimating ring-fault parameters of vertical-CLVD earthquakes, enabling us to examine the kinematics and structures below active volcanoes with ring faults that are distributed globally.

1 Introduction

Seismological methods can be used for the study of active volcanoes to investigate geometries of subsurface structures and the physics of fluid transport into the magma plumbing system. Observations and analyses of shallow earthquakes with volcanic origins provide information on stress levels in volcanic edifices caused by magmatic pressures ascending from depth. This information is important for predicting eruptions and assessing hazards related to volcanic activity (e.g., McNutt, 2002; Chouet, 2003; Kawakatsu and Yamamoto, 2015). In most cases, small earthquakes are analyzed with in situ or near-field observations to infer detailed dynamics of magma transport or brittle fractures of volcanoes; for example, Kilauea in Hawaii or Bárdarbunga in Iceland. In contrast, larger volcanic earthquakes are sometimes recorded by regional and global seismic networks (e.g., Kanamori and Given, 1982; Kanamori et al., 1982; Kanamori and Mori, 1992; Ekström, 1994; Shuler et al., 2013a). If seismic signals radiated by such earthquakes can be utilized, it is possible to study volcanoes distributed globally, including those on remote islands or underwater without local observation systems. These include the submarine Smith caldera, south of Japan, which causes volcanic earthquakes with seismic magnitudes of >5 (e.g., Kanamori et al., 1993; Fukao et al., 2018; Sandanbata et al., 2018), and submarine volcanic areas near Mayotte Island in the Comoro Islands, which showed significant seismicity during 2018–2019 (Cesca et al., 2020; Darnet et al., 2020).

One of the most notable types of volcanic earthquake observed at regional or global scales are those with seismic magnitudes of $M_w > 5$ that are characterized by moment tensors (MTs) having a dominant vertical compensated-linear-vector-dipole (vertical-CLVD) component (e.g., Kanamori et al., 1993; Ekström, 1994; Shuler et al., 2013a; 2013b). There are two types of vertical-CLVD earthquake: one contains a dominant tension axis (vertical-T CLVD earthquakes), and the other contains a dominant pressure axis (vertical-P CLVD earthquakes) (e.g., Ekström, 1994; Shuler et al., 2013a; 2013b) (Figure 1). Vertical-CLVD earthquakes cannot be explained by shear rupture on a planar fault (e.g., Frohlich, 1994; Ekström, 1994; Shuler et al., 2013b), indicating that their anomalous mechanisms are associated with complex source structures or magmatic processes. For vertical-CLVD earthquakes at volcanoes, several models have been proposed, including ring-faulting (e.g., Ekström, 1994), rapid water–magma interaction initiated by magma intrusion into shallow crust (Kanamori et al., 1993), and opening or closing of a horizontal crack (e.g., Riel et al., 2015; Fukao et al., 2018).

Among the different proposed source models, the ring-faulting mechanism explains many features of vertical-CLVD earthquakes (e.g., Ekström, 1994; Shuler et al., 2013a; 2013b). Ekström (1994) showed that MT analyses of long-period seismic signals that are radiated by pure dip slips on a curved ring fault result in vertical-CLVD focal mechanisms. Shuler et al. (2013a, 2013b) surveyed vertical-CLVD earthquakes near volcanoes from 1976 to 2009 and located their centroids within the top 10 km of the crust, which is consistent with the formation process of ring faults during caldera collapse (e.g., Cole et al., 2005; Acocella, 2007; Geyer and Martí, 2014). Those authors showed that most vertical-CLVD earthquakes were temporally associated with activity at nearby volcanoes with caldera structures. Vertical-CLVD earthquakes near Bárdarbunga in Iceland and Nyragongo in the Democratic Republic of the Congo have also been attributed to slips on non-planar ring faults (e.g., Gudmundsson et al., 2016; Parks et al., 2017; Nettles and Ekström, 1998; Shuler and Ekström, 2009). The recurrence of vertical-CLVD earthquakes at two shield volcanoes showing pronounced surface deformation or micro-seismicity along well-documented ring-fault structures has indicted their origins related to ring-faulting at the Rabaul caldera in Papua New Guinea (e.g., McKee et al., 1984; Mori and McKee, 1987; Mori et al., 1989; Shuler et al., 2013b) and the Sierra Negra caldera in the Galápagos Islands (e.g., Amelung et al., 2000; Yun et al., 2006; Yun, 2007; Jónsson, 2009).

MT inversion using long-period seismic waves has been applied to study the sources of vertical-CLVD earthquakes from far-field observations (e.g., Shuler et al., 2013b; Duputel and Rivera, 2019; Fontaine et al., 2019). Because of long-period properties, detailed 3D velocity structures of the volcanic edifices are not required. MT solutions of ring-faulting are known to reflect the properties of earthquake sources, such as the kinematics of a central block and the dip directions of a ring fault. As illustrated in Figure 1, when the central block moves upward on the inward-dipping ring fault (Figure 1a), or downward on the outward-dipping ring fault (Figure 1b), vertical-T CLVD earthquakes are produced; in contrast, if the kinematics of the block are reversed, vertical-P CLVD earthquakes are produced (Figure 1c and d). Hence, the polarity of the MT solutions (vertical-T or -P) helps to determine either the kinematics of the central block (upward or downward) or the dip direction of the ring fault (inward or downward), once either of the two is constrained from other observations such as crustal deformation or micro-seismicity (e.g., Shuler and Ekström, 2009; Gudmundsson et al., 2016).

However, it has proved challenging to relate MT solutions obtained from long-period seismic waves directly to ring-fault parameters such as arc angle, dip angle, and the location of slip along the ring fault. One of the reasons for the difficulty is that amplitudes of radiated long-period seismic waves are reduced owing to partial cancellations of long-period seismic waves from different portions of a ring fault (Ekström, 1994). Another reason is the instability of MT inversion for shallow earthquakes (e.g., Dziewonski et al., 1981; Kanamori and Given, 1981). Although Shuler et al. (2013b) related MT solutions obtained from long-period seismic records to ring-fault parameters using the plunge of the tension or pressure axis and a parameter representing the dominance of the non-double-couple component, their estimations were not always consistent with those observed in nature or in analog models. Contreras-Arratia and Neuberg (2020) showed that detailed ring-fault parameters can be recovered from near-field seismic stations with good azimuth coverage. However, once reliable relationships between ring-fault parameters and MT solutions obtained from long-period seismic records are established, MT inversion will be a more powerful tool to remotely study the kinematics and subsurface structures of active volcanoes distributed globally that cause ring-faulting.

The objective of this study is to find a robust way of estimating ring-fault parameters using the MT solutions of vertical-CLVD earthquakes. We first model theoretical MTs of idealized ring-faulting with variable ring-fault parameters and decompose them into MT components. Although the MT component representing the vertical dip-slip mechanism is difficult to determine with long-period seismic waves, we show that the remaining MT components can be used to estimate some ring-fault parameters. To validate the theoretical argument, we estimate the ring-fault parameters of vertical-CLVD earthquakes at the Sierra Negra caldera by investigating their resolvable components of MT solutions determined with long-period seismic waves and then compare the estimated parameters with those identified in previous studies using geodetic observations and field surveys. We also discuss possible bias in MT inversion caused by a seismic source with a volume change close to the ring-faulting.

2 Analysis

2.1 Modeling and decomposition of moment tensors of ring-faulting

In this section, we theoretically explore robust relationships between MTs and ring-fault parameters. We define several ring-fault parameters, namely, the arc angle Θ, the midpoint of the ruptured arc segment *M*, the ring-fault azimuth $\overrightarrow{OM}$, and the ring-fault orientation (Figure 2). The ring-fault orientation is normal to the ring-fault azimuth vector. The azimuth can vary from 0° to 360°, whereas the orientation can vary only from 0° to 180°.

Here we model theoretical MTs of ring-faulting in a similar way to Ekström (1994) and Shuler et al. (2013b). We discretize a curved ring fault into planar rhomboidal subfaults and define the MT of ring-faulting as the sum of the MTs of each subfault (Box 4.4 in Aki and Richards, 1980). As a ring fault is smaller than the wavelength, and the source time duration is shorter than the wave period of the long-period seismic waves that we use, the point-source approximation is valid. Here we consider idealized ring-faulting for a vertical-T CLVD mechanism: a reverse slip of 1 m along a circular inward-dipping ring fault (5 km radius at the surface) that extends from the surface to a depth of 2 km. We vary two ring-fault parameters, that is, the dip angle ranging from 45° to 90°, and the arc angle ranging from 0° to 360° (Figure 2a). Only vertical-T earthquakes are discussed here because MTs of vertical-P earthquakes can be examined by changing the signs of the MTs.

The scalar moment of the theoretical MTs is computed by following the definition given by Silver and Jordan (1982) and Dahlen and Tromp (1998):

$$M_0 = \sqrt{\Sigma_{ij} M_{ij} M_{ij} / 2}, \qquad (1)$$

where M_{ij} are the *ij* elements of an MT in spherical coordinates (r, θ, and ϕ) representing up, south, and east, respectively. The moment magnitude is computed as:

$$M_w = \frac{2}{3}\left(\log_{10} M_0 - 9.10\right). \qquad (2)$$

with M_0 being measured in N m (e.g., Kanamori, 1977; Hanks and Kanamori, 1979).

We next decompose the theoretical MTs in a similar way to Kawakatsu (1996). For the decomposition, we define three moment scales corresponding to isotropic (*ISO*), vertical-CLVD (*CLVD*), and difference (*D*) components with the three diagonal elements (M_{rr}, $M_{\theta\theta}$, and $M_{\phi\phi}$):

$$M_{ISO} = \frac{1}{3}\left(M_{rr} + M_{\theta\theta} + M_{\phi\phi}\right), \qquad (3)$$

$$M_{CLVD} = \frac{1}{3}\left(2M_{rr} - M_{\theta\theta} - M_{\phi\phi}\right), \qquad (4)$$

and

$$M_D = \frac{1}{2}\left(M_{\theta\theta} - M_{\phi\phi}\right). \qquad (5)$$

Note that for the MT of ring-faulting, no isotropic component is contained ($M_{ISO} = 0$). Hence, using the two moment scales (M_{CLVD} and M_D) and the non-diagonal elements ($M_{r\theta}$, $M_{r\phi}$, and $M_{\theta\phi}$), the MT of ring-faulting can be uniquely decomposed into three deviatoric MT components in the following form:

$$\boldsymbol{M} = \boldsymbol{M}_{CLVD} + \boldsymbol{M}_{SS} + \boldsymbol{M}_{DS}, \quad (6)$$

where

$$\boldsymbol{M}_{CLVD} = M_{CLVD} \begin{bmatrix} 1 & & \\ 0 & -0.5 & \\ 0 & 0 & -0.5 \end{bmatrix}, \quad (7)$$

$$\boldsymbol{M}_{SS} = \boldsymbol{M}_{D} + \boldsymbol{M}_{\theta\phi} = M_{D} \begin{bmatrix} 0 & & \\ 0 & 1 & \\ 0 & 0 & -1 \end{bmatrix} + M_{\theta\phi} \begin{bmatrix} 0 & & \\ 0 & 0 & \\ 0 & 1 & 0 \end{bmatrix}, \quad (8)$$

and

$$\boldsymbol{M}_{DS} = \boldsymbol{M}_{r\theta} + \boldsymbol{M}_{r\phi} = M_{r\theta} \begin{bmatrix} 0 & & \\ 1 & 0 & \\ 0 & 0 & 0 \end{bmatrix} + M_{r\phi} \begin{bmatrix} 0 & & \\ 0 & 0 & \\ 1 & 0 & 0 \end{bmatrix}. \quad (9)$$

The three components $\boldsymbol{M}_{CLVD}$, $\boldsymbol{M}_{SS}$, and $\boldsymbol{M}_{DS}$ represent different source types, which are the vertical-CLVD (*CLVD*), vertical strike-slip (*SS*), and vertical dip-slip (*DS*) components, respectively (Figure 2b). The sign of M_{CLVD} in Equation (7) depends on the type of vertical-CLVD earthquake: $M_{CLVD} > 0$ for vertical-T earthquakes, and $M_{CLVD} < 0$ for vertical-P earthquakes.

Using absolute values defined by $|M_{CLVD}|$, $M_{SS} = \sqrt{M_D^2 + M_{\theta\phi}^2}$, and $M_{DS} = \sqrt{M_{r\theta}^2 + M_{r\phi}^2}$, we can quantify the ratios of the *CLVD*, *SS*, and *DS* components in the MT of ring-faulting as:

$$\frac{|M_i|}{|M_{CLVD}| + M_{SS} + M_{DS}} \times 100\ [\%], \quad (10)$$

where *i* represents *CLVD*, *SS*, or *DS*.

Figures 2c and 2d show the theoretical MTs and components for reverse slips on ring faults with dip angles of 60° and 75° that extend along azimuthal arc angles of 90°, 180°, 270°, and 360° (2nd–5th rows, respectively). The ring-fault azimuths are 0°. For comparison, MTs of slips on planar faults with the same dip angles are shown (1st row). Ring-faulting has a vertical-CLVD mechanism, as long-period seismic contributions from different segments along the curved ring fault partially cancel out (Ekström, 1994). The geometric cancellation can be understood with the decomposition of theoretical MTs. The azimuths of principal axes for the two double-couple components, $\boldsymbol{M}_{SS}$ and $\boldsymbol{M}_{DS}$, are determined by the strike angle of a planar fault (1st row). Hence, the double-couple components from a portion of the ring fault cancel out those from another portion striking in a different azimuth. In contrast, as the *CLVD* component, $\boldsymbol{M}_{CLVD}$, of a planar fault does not change with its strike angle, the component of the ring fault accumulates and becomes more dominant in the moment tensor as the arc angle increases.

2.2 Indeterminate *DS* component at a shallow source depth

Once the MT solutions of ring-faulting are determined, the ring-fault parameters, namely, dip angle, arc angle, and ring-fault azimuth (Figure 2a), can be estimated from the ratios of the three components and azimuths of the principal axes of the *SS* and *DS* components. However, the *DS* component of such shallow earthquakes is known to be indeterminate with MT inversion using long-period seismic waves (e.g., Dziewonski et al., 1981; Kanamori and Given, 1981). The indeterminacy of the *DS* component of shallow earthquakes arises from its small contribution to long-period seismic waves, as the $r\theta$ and $r\phi$ elements of the strain tensor ($\varepsilon_{r\theta}$ and $\varepsilon_{r\phi}$) are nearly zero near the solid surface. To confirm the indeterminacy of the *DS* component at a shallow depth, we synthetize long-period (0.005–0.0125 Hz) seismic waveforms, including all of the relevant phases (e.g., P, S, and surface waves), at a virtual station from five hypothetical sources representing elementary components, $\boldsymbol{M}_{CLVD}$, $\boldsymbol{M}_{D}$, $\boldsymbol{M}_{\theta\phi}$, $\boldsymbol{M}_{r\theta}$, and $\boldsymbol{M}_{r\phi}$, with the same scalar moment $M_0 = 1.0 \times 10^{18}$ N m (M_w 5.9) using Equation (1) (Figure 3). Details of the numerical method used are described in the caption of Figure 3. For a source at 2.5 km depth, amplitudes of long-period seismic waves radiated from the *DS* component ($\boldsymbol{M}_{r\theta}$, $\boldsymbol{M}_{r\phi}$) are much smaller than those from the *CLVD* component ($\boldsymbol{M}_{CLVD}$) and the *SS* component ($\boldsymbol{M}_{D}$, $\boldsymbol{M}_{\theta\phi}$) (Figure 3a). Because of the inefficient seismic excitation, estimation of the *DS* component is unstable. Also, small errors in the depth of the source result in large uncertainties in the *DS* components owing to large variations in the amplitudes of synthetic long-period seismic waves. If the source is at 10.5 km depth, the *DS* component radiates larger seismic waves (Figure 3b).

The difficulty in determining the *DS* component of shallow earthquakes is encountered in MT inversion of tectonic earthquakes and leads to large uncertainties in the estimation of dip angle and seismic magnitude (e.g., Dziewonski et al., 1981; Kanamori and Given, 1981). Similarly, the indeterminacy makes it difficult to estimate important ring-fault parameters from long-period seismic waves. The dip angle and scalar moment of ring-faulting cannot be well constrained. In addition, we cannot determine the ring-fault azimuth, which is reflected in the azimuth of the tension axis of the *DS* component.

2.3 Resolvable MTs of ring-faulting

Given the indeterminacy of the *DS* component, we propose a method for estimating two ring-fault parameters using only the *CLVD* and *SS* components, which are resolvable with long-period seismic waves. Here we define the resolvable MT ($\boldsymbol{M}_{res}$) by:

$$\boldsymbol{M}_{res} = \boldsymbol{M}_{CLVD} + \boldsymbol{M}_{SS}. \qquad (11)$$

$\boldsymbol{M}_{res}$ for the idealized ring-faulting is shown in the 6th column in Figures 2c and 2d. Here, we introduce two new dimensionless physical parameters extracted from $\boldsymbol{M}_{res}$, as follows. The first parameter, k_{CLVD}, is the ratio of $|M_{CLVD}|$ to $|M_{CLVD}| + M_{SS}$ of $\boldsymbol{M}_{res}$ defined by:

$$k_{CLVD} = \frac{|M_{CLVD}|}{|M_{CLVD}|+M_{SS}} \times 100\ [\%], \qquad (12)$$

which we call the *CLVD ratio*. This parameter can be used to estimate the ring-fault arc angle Θ (Figure 4a). As Θ increases from 0° to 180°, k_{CLVD} increases from 66.7% to 100%. From Θ =180°, k_{CLVD} decreases to a local minimum of 90% at ~255°, and then increases to 100% at 360°. k_{CLVD} reaches 100% when Θ is 180° or 360°, where the *SS* component vanishes. The relationship between k_{CLVD} and Θ does not depend on the dip angle because pure dip slip on a planar fault with any dip angle in all cases results in the same *CLVD*-to-*SS* component ratio of 2:1 (top row in Figures 2c and 2d). Thus, we can use k_{CLVD} to estimate Θ even if the *DS* component is indeterminate.

The second parameter, ψ, is defined as follows. The resolvable moment tensor $\boldsymbol{M}_{res}$ discussed here is given by three orthogonal dipoles. We use the orientation of the dipole with the smallest absolute moment to estimate the orientation of the ring fault. As shown in Figures 2c and 2d (4th column), this dipole determines the elongation direction of the nodal-line pattern of the mechanism diagrams of $\boldsymbol{M}_{res}$. It can also be shown that this orientation is the same as the orientation of the Null (N) axis of the *best-fitting double-couple moment tensor* (pp. 248–251 of Shearer, 2009) shown by thin curves on the mechanism diagrams (4th column of Figures 2c and 2d). We refer to the dipole axis as the *N-axis* and denote its orientation by ψ, which is measured from the north, eastward-reckoned positive, $0 \leq \psi < 180°$. Figures 4b and 4c show the relationships between the ring-fault orientation and the N-axis for vertical-T and vertical-P CLVD earthquakes. The ring-fault orientation is parallel or perpendicular to the N-axis depending on $\Theta < 180°$ or $\Theta > 180°$, respectively. Because ψ is independent of the dip angle, this parameter can be used to estimate the ring-fault orientation without knowing the *DS* component. We note that what can be estimated from ψ is not the ring-fault azimuth but the orientation (Figure 2); we cannot distinguish two different ring faults with the same arc angle but rotated by 180° to each other.

Thus, $\boldsymbol{M}_{res}$ for shallow ring-faulting is useful for estimating ring-fault parameters by using k_{CLVD} and ψ together. If k_{CLVD} is less than ~90%, Θ can be uniquely determined by k_{CLVD} because Θ is a single-valued function of k_{CLVD} (Figure 4a). In this case, the ring-fault orientation is parallel to the N-axis (Figures 4b and 4c). In contrast, if k_{CLVD} is larger than ~90%, Θ cannot be determined uniquely and three values of Θ are possible for a given k_{CLVD} (Figure 4a); there also remain two possibilities for the ring-fault orientation, parallel or perpendicular to the N-axis, depending on Θ (Figures 4b and 4c). When $\Theta = 180°$, the N-axis orientation is indeterminate (Figures 2c and 2d), and the ring-fault orientation cannot be determined. When $\Theta = 360°$, the ring-fault orientation is irrelevant.

3 Case study: Vertical-CLVD earthquakes at the Sierra Negra caldera, Galápagos Islands

In the previous section, we showed that the resolvable MTs, $\boldsymbol{M}_{res}$, which are composed of the *CLVD* and *SS* components, of ring-faulting are useful for estimating the arc angle Θ and the orientation of the ring fault. Here, we investigate the relationships for a vertical-CLVD earthquake that occurred at the Sierra Negra caldera prior to the 2005 volcanic activity. We first test the stability of $\boldsymbol{M}_{res}$ obtained from MT inversion using long-period seismic records at far field. Then, we analyze $\boldsymbol{M}_{res}$ to estimate the ring-fault parameters and compare them with other observations. We also investigate two vertical-CLVD earthquakes during volcanic activity in 2018.

3.1 M_w 5.5 vertical-T CLVD earthquake prior to the 2005 eruption

The Sierra Negra is a shield volcano located at the southern end of Isabella Island, in the Galápagos Islands (Figure 5a). A shallow 7 km × 10.5 km caldera structure is formed at the summit of the 1124-m-high volcano (Figure 5b; Reynolds et al., 1995). On 22 October 2005, the Sierra Negra caldera started eruption activity at ~23:30 in UTC (e.g., Global Volcanism Project, 2005; Geist et al., 2008). At 20:34 on the same day, about 3 h before initiation of the eruption, a vertical-T CLVD earthquake with M_w 5.5 occurred (Chadwick et al., 2006; Jónsson, 2009). Clear long-period seismic signals from this earthquake were observed at far-field stations (black curves in Figure 6). Geodetic observations using data obtained from Global Positioning System (GPS) and Interferometric Synthetic Aperture Radar (InSAR) suggested reverse slips along a sinuous fault system with an inward dip angle on the western to southern parts of the caldera caused by a pressurized sill-like magma chamber lying at a depth of about 2 km (Jónsson, 2009). This fault-motion mechanism is termed *trapdoor faulting* (e.g., Amelung et al., 2000; Chadwick et al., 2006; Jónsson, 2009). The mechanism was indicated by a fresh fault scarp (dashed and solid curves in Figure 5b) identified by Geist et al. (2008), who conducted field surveys at the caldera after the 2005 eruption. The shallow sill-like magma chamber estimated from geodetic data (Jónsson, 2009) suggests that the earthquake occurred in the top ~2 km of the crust. For this geometry at such a shallow depth, the indeterminacy of the *DS* component is an issue. Thus, this is a good example for investigating how the MT solution of a vertical-CLVD earthquake caused by ring-faulting is related to the geometry of the ring fault identified by geodetic studies and field surveys.

3.2 Data & methods

We perform MT inversion for the M_w 5.5 vertical-T earthquake near the Sierra Negra caldera. We use the W-phase code for the inversion, including filtering, data screening, and convolution of Green's functions (Kanamori and Rivera, 2008; Hayes et al., 2009; Duputel et al., 2012). We use the normal mode method (e.g., Takeuchi and Saito, 1972) to compute Green's functions for the 1-D Preliminary Reference Earth Model (PREM; Dziewonski and Anderson, 1981), in the same way as we did for the synthetic test in Section 2.2. Long-period seismic waves are extracted from synthetic and observed waveforms by applying a one-pass, fourth-order Butterworth bandpass filter with corner frequencies at 0.005 and 0.0125 Hz. The inversion time window is set to include P, S, and surface waves. We assume zero contribution by a volume change to the long-period seismic waves by imposing the zero-trace constraint, $M_{rr} + M_{\theta\theta} + M_{\phi\phi} = 0$. This means that the seismic waves are entirely attributed to ring-faulting. Possible bias caused by a volume change is discussed later in Section 4.2.

We use long-period seismic records at far-field stations for the inversion. We download seismic records at far-field stations within 5°–60° of the epicentral distance as obtained from the Data Management Center of the Incorporated Research Institutions for Seismology (IRIS). To remove bad data (i.e., data with glitch, or low signal-to-noise ratio), we conduct a trial MT inversion using a source placed at 2.5 km depth in the crust just below the Sierra Negra caldera (0.83°S, 91.14°W), assuming the centroid time shift and half duration reported in the Global Centroid Moment Tensor (GCMT) Catalog. Using the result of the trial inversion, we select 25 seismic records with a root mean square (RMS) misfit smaller than 0.9; the RMS is defined by $\rho_i = \|\boldsymbol{s}_w^i - \boldsymbol{d}_w^i\| / \|\boldsymbol{s}_w^i\|$, where $\boldsymbol{s}_w^i$ and $\boldsymbol{d}_w^i$ are synthetic and observed data in the inversion time window at the $\boldsymbol{i}$-th station, respectively, and $\|\boldsymbol{s}\|$ represents the L2 norm of data vector $\boldsymbol{s}$. The selected dataset is for the epicentral distance range from 12.4° to 46.6° and has a good azimuthal coverage (Figure 6). The stations are from different seismic networks: the Global Seismograph Network (II, IU), Broadband Tomography Under Costa Rica and Nicaragua (YO, 2003–2006), GEOSCOPE (G), and the United States National Seismic Network (US).

To examine the stability of the MT solutions, we repeat MT inversion while moving the centroid location in a 3D space around the Sierra Negra caldera. By examining the variation in the MT solutions, we can assess the sensitivity of the solutions to small variations in estimated centroid location, noise in the data, model imperfections, and unmodeled subsurface velocity structures. For MT inversion in 3D space, centroid locations are distributed on two planes: the x–y (longitude–latitude) plane at a depth of 2.5 km in the crust (Figure 7a), and the x–z (longitude–depth) plane along a latitude of 0.83°S across the caldera (Figure 7b). The centroid location intervals are 0.1° in the horizontal direction and 2.0 km in the vertical direction. At each centroid location, we conduct MT inversion while grid-searching an optimal value of the centroid time shift, assuming the half duration to be the same as the centroid time shift. The waveform fit for the MT solution is measured with the normalized RMS (NRMS) misfit, $\Sigma_{i=1}^{N}(\rho_i/N)$, where *N* is the number of seismic records, and ρ_i is the RMS misfit at the ***i***-th station. Then, we set $M_{r\theta} = M_{r\phi} = 0$ for the obtained MT solutions to estimate $\boldsymbol{M}_{res}$ defined by Equation (11). Strictly speaking, to estimate $\boldsymbol{M}_{res}$ exactly with the constraint of $M_{r\theta} = M_{r\phi} = 0$, we need to perform three-element MT inversions with the three constraints, $M_{r\theta} = M_{r\phi} = 0$, and $M_{rr} + M_{\theta\theta} + M_{\phi\phi} = 0$. However, to compare our solutions with the GCMT solutions which were obtained for the five MT elements with the only constraint $M_{rr} + M_{\theta\theta} + M_{\phi\phi} = 0$, we here perform five-element MT inversions only with the constraint $M_{rr} + M_{\theta\theta} + M_{\phi\phi} = 0$, and after the solution was obtained we set $M_{r\theta} = M_{r\phi} = 0$. In Supporting Information, we compare $\boldsymbol{M}_{res}$ obtained with these two methods and show that the results are very similar when the datasets are good.

3.3 Results

3.3.1 Indeterminate *DS* component and stability of the resolvable MT

Figure 7a shows NRMS values for the MT solutions at locations on the x–y plane at a depth of 2.5 km. In the area around the Sierra Negra caldera (white rectangle in Figure 7a), NRMS values are small. Figure 7b shows NRMS values for the MT solutions on the x–z plane along latitude 0.83°S (dashed line in Figure 7a). Similarly, small NRMS values are given by most MT solutions in the top ~15 km of the crust. For example, the MT solution at the caldera (0.83°S, 91.14°W; red circle in Figure 7a) at a depth of 2.5 km reproduces the observed records well with an NRMS value of 0.365 (Figure 6). From the MT solutions in 3D space, 53 solutions at different centroid grids yield NRMS values of ≤0.365, which we refer to as *acceptable solutions* hereafter.

Figure 7c shows the MT solutions on the x–y plane at a depth of 2.5 km in the area around the caldera (white rectangle in Figure 7a), and Figure 7d shows them on the x–z plane along a latitude of 0.83°S (white dashed line in Figure 7a) in the top ~10 km of the crust. The solutions on the two planes differ significantly depending on centroid locations in the 3D space, although they yield similar small NRMS values. Notably, at shallower depths in the crust, estimated M_w values and ratios of the *DS* component are larger (Figure 7d). For the 53 acceptable solutions, M_W values are distributed widely from 5.50 to 6.49 (Figure 8a), and the ratio of the *DS* component, computed with Equation (10), ranges from 44.8% to 97.7% (Figure 8b). These results demonstrate the instability of MT inversion caused by the indeterminate *DS* component discussed in Section 2.2.

From the MT solutions at centroid locations on the x–y and x–z planes, we extract $\boldsymbol{M}_{res}$ defined by Equation (11) (Figures 7e and 7f). $\boldsymbol{M}_{res}$ on the two planes have similar focal mechanisms and M_W. M_W values are in a narrow range (5.33 ± 0.04) for the 53 acceptable solutions (Figure 8c). Also, $\boldsymbol{M}_{res}$ for the acceptable solutions contain stable values of the CLVD ratio k_{CLVD} (73.0% ± 3.0%; Figure 8d) and the N-axis azimuth ψ (102.7° ± 3.0°; Figure 8e). These results confirm that $\boldsymbol{M}_{res}$ is stably obtained for vertical-CLVD earthquakes, even in the cases where centroid locations are not accurately determined, indicating its stability under the presence of noise in observed data, and in cases where there are imperfections in simulation models or velocity structures. Therefore, we reemphasize that the two physical parameters (i.e., k_{CLVD} and ψ) obtained from $\boldsymbol{M}_{res}$ can be used to reliably estimate ring-fault parameters.

In Figure 9 and Table 1, we compare the MT solution obtained for the centroid location at a depth of 2.5 km just below the caldera (0.83°S, 91.14°W) with the solution from the GCMT Catalog. The centroid depth of the GCMT solution is 12.0 km. The two MT solutions, including the indeterminate *DS* component, have very different focal mechanisms, M_W values, and ratios of the *DS* component (Figures 9a and 9b). In contrast, $\boldsymbol{M}_{res}$ extracted from the two different solutions show similar values for M_w (5.31 and 5.31), k_{CLVD} (73.4% and 77.3%), and ψ (101.9° and 96.3°; Figures 9c and 9d). These results demonstrate that $\boldsymbol{M}_{res}$ can be reliably estimated from various available catalogs such as the GCMT, even if the centroid depth and the complete MT are not accurately determined for shallow earthquakes (e.g., Chu et al., 2009; Wimpenny and Watson, 2020).

3.3.2 Ring-fault parameters inferred from the resolvable MT

We next estimate ring-fault parameters for the 2005 vertical-T CLVD earthquake at the Sierra Negra caldera from $\boldsymbol{M}_{res}$ of the MT solution (Figure 9c). If we assume that the seismic waves are generated entirely from idealized ring-faulting (uniform slip along a circular ring fault), $\boldsymbol{M}_{res}$ with a value of k_{CLVD} of 73.4% indicates a ring fault extending along an arc angle Θ of ~80° (Figure 4a). In such a case of $\Theta < 180°$, the N-axis with ψ of 101.9° suggests that the ring-fault orientation is a direction rotated slightly clockwise from the E–W. On the other hand, the intra-caldera fault (black curve in Figure 5b), which was attributed to the earthquake source (Amelung et al., 2000; Chadwick et al., 2006; Jónsson, 2009), has an arc angle a little smaller than 90° and its orientation is slightly rotated clockwise from the E–W, if we approximate the fault as a circular arc. Although here we do not consider complexities of the actual fault geometry and slip distributions, the overall agreement of the ring-fault parameters with the well-documented intra-caldera fault geometry strongly suggests that we can study geometries of ring faults at volcanoes by analyzing the $\boldsymbol{M}_{res}$ of MT solutions obtained from long-period seismic records at far field.

3.4 Insights into two vertical-CLVD earthquakes prior to and during the 2018 eruption

The Sierra Negra caldera renewed its eruption activity at ~19:40 on 26 June 2018 (UTC), which lasted until 23 August (Global Volcanism Program, 2018; Vasconez et al., 2018). The activity included fissure eruptions from several fissure vents along the northern part of the caldera rim and on the northern side of the volcanic flank, and large volcanic deformations with increased seismicity at the caldera. Prior to and during the eruption, two vertical-CLVD earthquakes with $M_w > 5$ were reported near the Sierra Negra caldera: an M_w 5.3 earthquake at 9:15 on 26 June, about 10 h before the initiation of the eruption, and an M_w 5.1 earthquake at 0:30 on 5 July. The two earthquakes were attributed to trapdoor faulting events on the intra-caldera fault structure by La Femina et al. (2018), who analyzed GPS records at the caldera. This indicates the ring-faulting origin of the earthquakes.

To provide insights into the sources of two vertical-CLVD earthquakes, we here analyze their MT solutions from the GCMT Catalog (Table 1, Figures 10a and 10c). A vertical-T earthquake occurred on 26 July before the eruption (Figure 10a), and a vertical-P earthquake on 5 July after the eruption started (Figure 10c). Focal mechanisms and the parameters (k_{CLVD} and ψ) of $\boldsymbol{M}_{res}$ extracted from the MT solutions of the vertical-T and P earthquakes are shown in Figures 10b and 10d, respectively. For the vertical-T earthquake, k_{CLVD} is 72.2% and ψ is 86.4° (approximately E–W), and for the vertical-P earthquake, k_{CLVD} is 71.9% and ψ is 55.5° (approximately NE–SW).

Here we suggest source kinematics and geometries of the earthquakes from the GCMT solutions together with pre- and co-seismic deformation reported by La Femina et al. (2018). First, the difference in the types of vertical-CLVD earthquake (vertical-T or -P) may be explained by flipped kinematics of slips on inward-dipping ring faults. La Femina et al. (2018) reported that the first (vertical-T) earthquake took place during the inflation phase of the caldera, preceding the eruption, whereas the second (vertical-P) earthquake occurred during a rapid deflation phase that began following the initiation of the eruption. Considering the co-seismic deformation patterns of the caldera at the times of the earthquakes, it is reasonable to attribute the vertical-T earthquake during the inflation phase to upward motion of the central block along an inward-dipping ring fault (Figure 1a), and the vertical-P earthquake during the deflation phase to a drop of the block slipping on an inward-dipping ring fault (Figure 1c).

On the basis of $\boldsymbol{M}_{res}$ values of the GCMT solutions, we further investigate ring-fault parameters of the two vertical-CLVD earthquakes. The small values of k_{CLVD}, 72.2% for the vertical-T earthquake and 71.9% for the vertical-P earthquake (Figures 10b and 10d), indicate that both earthquakes occurred along short ring faults with arc angles Θ of ~80°, according to the relationship between k_{CLVD} and Θ (Figure 4a). In contrast, the significant difference in ψ of ~31° (compare Figures 10b and 10d) implies that the earthquakes occurred on different segments of the intra-caldera fault system. On the basis of the relationship between the N-axis of $\boldsymbol{M}_{res}$ and the orientation of the ring fault with $\Theta < 180°$ (top row in Figure 4b), the N-axis of $\boldsymbol{M}_{res}$ is expected to be parallel to the ring-fault orientation. Therefore, we suggest that the vertical-T earthquake occurred on a ring fault oriented in the E–W direction, whereas the vertical-P earthquake occurred on a different ring-fault segment oriented in the NE–SW direction. La Femina et al. (2018) suggested that co-seismic deformation occurred in the western caldera at the times of the two earthquakes. This implies that ring-faulting occurred somewhere along the western half of the intra-caldera fault system. Given the fault structures exposed at the surface in the western half of the caldera (Figure 5b), we suggest that the vertical-T earthquake was generated by reverse slip on a southern intra-caldera fault oriented in the E–W direction, which may correspond to the southeastern part of the fault estimated as generating the 2005 earthquake (the southeastern part of the black curve in Figure 5b). By contrast, we infer that the vertical-P earthquake occurred on a ring-fault segment oriented in the NE–SW direction in the northwestern part of the caldera. For reference, we indicate a possible example of such ring-fault geometry that may have generated the vertical-P earthquake by a dashed white curve in Figure 5b. We emphasize that these ring-fault geometries need to be investigated together with other observations such as co-seismic deformation or near-field seismic waves. Although some uncertainties remain, we suggest that the clear differences between the parameters of $\boldsymbol{M}_{res}$ for the two vertical-CLVD earthquakes offer information about significant differences in slip kinematics and source locations along the intra-caldera fault system.

4 Discussion

4.1 Efficiency of long-period seismic excitation from ring-faulting

As demonstrated above, the nature of seismic excitation from ring-faulting is very different from that of regular tectonic earthquakes. In general, despite the spectacular surface expression of ring faults, the seismic excitation, especially at long periods (greater than ~100 s), is inefficient, which often causes difficulty in interpretation. We have already discussed several specific cases above, and here we add some general discussion to clarify the problem of the inefficient seismic excitation.

There are two aspects to this problem. First, as previously discussed by Ekström (1994) and Shuler et al. (2013b), the ring-fault geometry results in cancellation of the source strength, as measured by the scalar moment. As discussed in Section 2, we represent the MT of ring-faulting by the sum of MTs of planar rhomboidal subfaults under the point-source approximation. We then compute the scalar moment M_0 of the ring-faulting using Equation (1). Figure 11a shows the ratio:

$$\frac{M_0}{\sum_i \Delta M_0^i} \qquad (13)$$

as a function of the dip and arc angles, where ΔM_0^i is the scalar moment of the i-th subfault along the ring fault computed using Equation (1). This ratio is generally smaller than 1 owing to the geometrical cancellation of the double-couple components (i.e., $\boldsymbol{M}_{SS}$ and $\boldsymbol{M}_{DS}$).

In addition to this geometrical cancellation, the efficiency of seismic excitation of ring-faulting is reduced because of its shallow source property. As expressed by Equation (6), the MT of ring-faulting can be expressed by the sum of three components, $\boldsymbol{M}_{CLVD}$, $\boldsymbol{M}_{SS}$, and $\boldsymbol{M}_{DS}$. Because of the very shallow depth, $\boldsymbol{M}_{DS}$ does not contribute to seismic excitation; by contrast, the other two components ($\boldsymbol{M}_{CLVD}$, $\boldsymbol{M}_{SS}$), which we referred to as resolvable components, have contributions to seismic excitation. The effect of little or no seismic property of $\boldsymbol{M}_{DS}$ can be expressed by the following ratio of scalar moment of $\boldsymbol{M}_{\boldsymbol{res}}$ to that of the theoretical MT (Figure 11b):

$$\frac{M_0^{res}}{M_0}, \qquad (14)$$

where M_0^{res} is the scalar moment based on Equation (1) for $\boldsymbol{M}_{res}$ (defined by Equation (11)).

Then, the combined effect can be given by the ratio (Figure 11c):

$$\frac{M_0}{\sum_i \Delta M_0^i} \times \frac{M_0^{res}}{M_0} = \frac{M_0^{res}}{\sum_i \Delta M_0^i}. \qquad (15)$$

As shown in Figure 11c, the excitation efficiency of long-period seismic waves from ring-faulting at a shallow depth is generally low, being lower for ring faults dipping more steeply.

The inefficient excitation of long-period seismic waves explains many peculiar characteristics of vertical-CLVD earthquakes. Ring-faulting may generate greater surface deformation than expected empirically from their seismic magnitudes estimated with long-period seismic waves. This may explain the discrepancy between seismic magnitudes estimated for slip on the intra-caldera fault at the Sierra Negra caldera from geodetic and seismic data (Jónsson, 2009). If vertical-T CLVD earthquakes at submarine volcanoes near Torishima Island in Japan (Satake and Kanamori, 1991; Fukao et al., 2018) and near Curtis Island in New Zealand (Gusman et al., 2020) are related to ring-faulting, the disproportionately large tsunamis for their seismic magnitudes may be partially a result of the inefficient seismic excitation. Kanamori et al. (1993) identified an azimuthally uniform radiation pattern of Rayleigh waves and an absence of Love waves from a vertical-T earthquake. This peculiarity can also be explained by the geometrical cancellation of the double-couple components and inefficient excitation of the *DS* component.

4.2 Effect of volume change on the zero-trace estimate of the *CLVD* component

In previous sections, we estimated the CLVD moment scale M_{CLVD} of ring-faulting, defined by Equation (4), at a very shallow depth, with the assumption of a vanishing isotropic component M_{ISO}, defined by Equation (3). If a volume change occurs near ring-faulting, the estimated M_{CLVD} might be biased. As the bias depends on the geometry of the magma reservoir, we discuss three cases below.

<u>Horizontal tensile crack</u>

The moment tensor for a horizontal tensile (or compressional) crack with a volume change ΔV is given in the $(r,\ \theta,\ \phi)$ coordinate system by (e.g., Kawakatsu and Yamamoto, 2015)

$$\boldsymbol{M}_{Tensile} = \Delta V \begin{bmatrix} \lambda + 2\mu & & \\ 0 & \lambda & \\ 0 & 0 & \lambda \end{bmatrix}. \qquad (16)$$

As seismic excitation of a moment tensor $\boldsymbol{M}$ is determined by $(\boldsymbol{M}:\boldsymbol{\varepsilon})$, where $\boldsymbol{\varepsilon}$ is the strain tensor at the source (Gilbert, 1971), the excitation by the horizontal tensile crack is proportional to $(\lambda + 2\mu)\varepsilon_{rr} + \lambda\varepsilon_{\theta\theta} + \lambda\varepsilon_{\phi\phi}$, which is equal to σ_{rr}, where ε_{rr}, $\varepsilon_{\theta\theta}$, and $\varepsilon_{\phi\phi}$ are the rr, $\theta\theta$, and $\phi\phi$ elements of the strain tensor, respectively, and σ_{rr} is the rr element of the stress tensor. For a very shallow source, $\sigma_{rr} \approx 0$. This means that a very shallow horizontal tensile crack has no or little seismic excitation (pp. 180–183 of Dahlen and Tromp, 1998; Fukao et al., 2018).

Previous studies have suggested that the Sierra Negra caldera has a sill-like magma reservoir at a depth of ~2 km (e.g., Amelung et al., 2000; Chadwick et al., 2006; Jónsson, 2009). Because a volume change of such a shallow sill-like reservoir involves a moment tensor defined by Equation (16) and does not contribute to long-period seismic waves, it is reasonable to attribute the seismic waves from the vertical-CLVD earthquakes at the caldera only to ring-faulting, as done in Section 3.

The case for a horizontal tensile crack has an important implication for other types of volume change. $\boldsymbol{M}_{Tensile}$ can be decomposed as:

$$\Delta V \begin{bmatrix} \lambda + 2\mu & & \\ 0 & \lambda & \\ 0 & 0 & \lambda \end{bmatrix} = \left(\lambda + \frac{2}{3}\mu\right) \Delta V \begin{bmatrix} 1 & & \\ 0 & 1 & \\ 0 & 0 & 1 \end{bmatrix} + \frac{4}{3}\mu\, \Delta V \begin{bmatrix} 1 & & \\ 0 & -0.5 & \\ 0 & 0 & -0.5 \end{bmatrix}. \qquad (17)$$

The first and second terms on the right-hand side represent isotropic and CLVD sources, respectively. Thus, the vanishing excitation by a horizontal tensile crack simply means that a unit isotropic tensor $\begin{bmatrix} 1 & & \\ 0 & 1 & \\ 0 & 0 & 1 \end{bmatrix}$ is equivalent to a CLVD tensor $-\frac{4\mu}{3\lambda+2\mu} \begin{bmatrix} 1 & & \\ 0 & -0.5 & \\ 0 & 0 & -0.5 \end{bmatrix}$ for seismic excitation at a very shallow depth.

<u>Spherical source</u>

If the deformation below ring-faulting is represented by a spherical source given by a moment tensor

$$\boldsymbol{M}_{Sphere} = \Delta V \begin{bmatrix} \lambda + \frac{2}{3}\mu & & \\ 0 & \lambda + \frac{2}{3}\mu & \\ 0 & 0 & \lambda + \frac{2}{3}\mu \end{bmatrix} = \left(\lambda + \frac{2}{3}\mu\right) \Delta V \begin{bmatrix} 1 & & \\ 0 & 1 & \\ 0 & 0 & 1 \end{bmatrix} =$$

$$M_{ISO}^{Sphere} \begin{bmatrix} 1 & & \\ 0 & 1 & \\ 0 & 0 & 1 \end{bmatrix}, \qquad (18)$$

where

$$M_{ISO}^{Sphere} = \left(\lambda + \frac{2}{3}\mu\right) \Delta V, \qquad (19)$$

then, using the equivalence relation between the isotropic and CLVD tensors, the CLVD moment scale of ring-faulting at a shallow depth is observed as a CLVD source with

$$M'_{CLVD} = M_{CLVD} - \frac{4\mu}{3\lambda+2\mu} M_{ISO}^{Sphere} = M_{CLVD} - \frac{4}{3}\mu\,\Delta V. \qquad (20)$$

Thus, to estimate M_{CLVD} for ring-faulting, we need to add $\frac{4}{3}\mu\,\Delta V$ to the observed M'_{CLVD} estimated with the assumption of $\Delta V = 0$.

<u>Vertical cylindrical source</u>

If the deformation below ring-faulting is represented by a vertical cylindrical source given by a moment tensor

$$\boldsymbol{M}_{Cylinder} = \Delta V \begin{bmatrix} \lambda & & \\ 0 & \lambda + \mu & \\ 0 & 0 & \lambda + \mu \end{bmatrix} = \left(-\frac{2}{3}\mu\,\Delta V\right) \begin{bmatrix} 1 & & \\ 0 & -0.5 & \\ 0 & 0 & -0.5 \end{bmatrix} + \left(\lambda + \frac{2}{3}\mu\right) \Delta V \begin{bmatrix} 1 & & \\ 0 & 1 & \\ 0 & 0 & 1 \end{bmatrix}$$

$$= M_{CLVD}^{Cylinder} \begin{bmatrix} 1 & & \\ 0 & -0.5 & \\ 0 & 0 & -0.5 \end{bmatrix} + M_{ISO}^{Cylinder} \begin{bmatrix} 1 & & \\ 0 & 1 & \\ 0 & 0 & 1 \end{bmatrix}, \qquad (21)$$

where

$$M_{CLVD}^{Cylinder} = -\frac{2}{3}\mu\,\Delta V \quad (22)$$

and

$$M_{ISO}^{Cylinder} = \left(\lambda + \frac{2}{3}\mu\right)\Delta V, \quad (23)$$

then, considering the additional isotropic and CLVD components from the vertical cylindrical source, the CLVD moment scale of ring-faulting is equivalent to a CLVD source with

$$M'_{CLVD} = M_{CLVD} + \left(M_{CLVD}^{Cylinder} - \frac{4\mu}{3\lambda+2\mu} M_{ISO}^{Cylinder}\right)$$

$$= M_{CLVD} + \left\{-\frac{2}{3}\mu\,\Delta V - \frac{4\mu}{3\lambda+2\mu}\left(\lambda + \frac{2}{3}\mu\right)\Delta V\right\}$$

$$= M_{CLVD} - 2\mu\,\Delta V. \qquad (24)$$

Thus, we need to add $2\mu\,\Delta V$ to the observed M'_{CLVD} to estimate M_{CLVD} for ring-faulting.

To illustrate the equivalence relation between the isotropic and CLVD tensors discussed above, we show synthetic long-period waveforms computed for a CLVD source, an isotropic source, and a horizontal tensile crack source (Figure 12). For this comparison, we use a common metric for $\boldsymbol{M}_{CLVD}$, $\boldsymbol{M}_{ISO}$, and $\boldsymbol{M}_{Tensile}$. If we use the definition of a scalar moment M_0, given by Equation (1), then a CLVD source, $\begin{bmatrix} 1 & & \\ 0 & -0.5 & \\ 0 & 0 & -0.5 \end{bmatrix}$, an isotropic source, $\begin{bmatrix} 1 & & \\ 0 & 1 & \\ 0 & 0 & 1 \end{bmatrix}$, and a horizontal tensile crack source, $\begin{bmatrix} \lambda+2\mu & & \\ 0 & \lambda & \\ 0 & 0 & \lambda \end{bmatrix}$, can be written, respectively, as

$$M_0 \begin{bmatrix} \sqrt{4/3} & & \\ 0 & -\sqrt{1/3} & \\ 0 & 0 & -\sqrt{1/3} \end{bmatrix}, \qquad (25)$$

$$M_0 \begin{bmatrix} \sqrt{2/3} & & \\ 0 & \sqrt{2/3} & \\ 0 & 0 & \sqrt{2/3} \end{bmatrix}, \qquad (26)$$

and

$$M_0 \sqrt{\frac{2}{(\lambda+2\mu)^2+2\lambda^2}} \begin{bmatrix} \lambda+2\mu & & \\ 0 & \lambda & \\ 0 & 0 & \lambda \end{bmatrix}. \qquad (27)$$

Here, we use the same scalar moment of $M_0 = 1.0 \times 10^{18}$ Nm (M_w 5.9). The waveforms for the CLVD and isotropic sources are quite similar to each other, except for the polarity and amplitude (Figures 12a and 12b). Figure 12c shows waveforms for the horizontal tensile source. The amplitudes are very small, reflecting the cancellation effects of $\boldsymbol{M}_{CLVD}$ and $\boldsymbol{M}_{ISO}$.

5. Conclusions

In previous studies, vertical-CLVD earthquakes were attributed to ring-faulting at active volcanoes. However, the relationship between detailed ring-fault parameters and their MT solutions obtained from long-period seismic waveforms has been poorly understood. In Section 2, we showed theoretically that the main cause of the difficulty in relating them is the instability of MT inversion for earthquakes in the top part (shallower than ~10 km) of the crust due to inefficient excitation of seismic waves from some components. We then proposed reliable relationships of MT solutions with ring-fault parameters based on two physical parameters, namely, the CLVD ratio k_{CLVD} and the N-axis azimuth ψ, of the resolvable MT $\boldsymbol{M}_{res}$, which is composed of the vertical-CLVD and vertical strike-slip components. In Section 3, through a case study of the 2005 vertical-CLVD earthquake at the Sierra

Negra caldera, we verified the stability of $\boldsymbol{M}_{res}$ obtained by MT inversion using long-period seismic records at far field. We also demonstrated that the ring-fault parameters estimated with $\boldsymbol{M}_{res}$ were consistent with the geometry of the ring fault identified by geodetic observations and field surveys. In addition, we pointed out a clear difference between $\boldsymbol{M}_{res}$ values of two vertical-CLVD earthquakes during the 2018 activity at the caldera and proposed significant differences in the kinematics and source locations of the two ring-faulting events.

The present study demonstrates the usefulness of MT inversion using long-period seismic waveforms for investigating the slip kinematics and geometries of ring faults at active volcanoes, particularly those with caldera structures. Analyses of long-period seismic records at far field allow remote estimation of ring-fault parameters at active volcanoes even without local observation networks or detailed 3D velocity structure. At a wider scale, vertical-CLVD earthquakes have been observed at tens of active volcanoes (e.g., Shuler et al., 2013a; 2013b). Large seismic events with vertical-CLVD components can be used to investigate the ring-fault systems of remote volcanoes including not only well-monitored volcanoes, such as Kilauea (e.g., Neal et al., 2019; Tepp et al., 2020) and Bárdarbunga (e.g., Gudmundsson et al., 2016; Riel et al., 2015), but also remote volcanic islands or submarine volcanoes, whose activities cannot be investigated easily, such as the Smith caldera (Satake and Kanamori, 1991; Kanamori et al., 1993, Fukao et al., 2018) and Curtis Island, north of New Zealand (Gusman et al., 2020).

However, limitations of seismological investigations for vertical-CLVD earthquakes using long-period seismic records at far field remain. Some moment tensor elements of ring-faulting are inefficient for generating long-period seismic waves, so that parts of source parameters cannot be fully determined only from the records. The temporal–spatial history of rupture propagation along a fault may not be resolved owing to the long-period property. It is also difficult to constrain a source with a volume change accompanying ring-faulting. To recover more information regarding ring-faulting, shorter-period seismic waves may be utilized with heterogeneous 3-D velocity structures around the calderas (e.g., Contreras-Arratia and Neuberg, 2019; Hejrani and Tkalčić, 2019). Combinations of seismic analyses with other observations may also provide more details about fracture processes of earthquakes involving ruptures of subsurface fault systems and fluid or gas transportation. To constrain the mechanism of a source with a change in volume, geodetic observations of surface deformation using such as GPS, tiltmeters, or InSAR are commonly required (e.g., Yun, 2007; Anderson et al., 2019; Segall et al., 2019, 2020). Such improvements in seismological investigations and combinations with other geophysical observation techniques have the potential to broaden our knowledge about active volcanoes generating ring-faulting. A better understanding of vertical-CLVD earthquakes will provide insights into the interaction of subsurface volcanic processes with fault systems of volcanic edifices and magmatic processes, potentially leading to assessments of volcanic hazards.

Acknowledgments

We thank K. Nishida, S. Takemura, and T. Saito for helpful discussion. This work is funded by the JSPS KAKENHI (grant numbers JP17J02919, JP20J01689, and JP19K04034) and by the JST J-RAPID (grant number JPMJJR1805). O.S.'s travel to California Institute of Technology was supported by the Oversea Internship Program of Earthquake Research Institute, the University of Tokyo.

This manuscript has been edited by Stallard Scientific Editing (https://www.stallardediting.com/).

Data Availability Statement

We used topography and bathymetry data downloaded from the Advance Land Observation Satellite (ALOS) World 3D–30 m DEM (AW3D30; available from https://www.eorc.jaxa.jp/ALOS/en/index.htm) provided by the Japan Aerospace Exploration Agency (JAXA), and from GEBCO_2020 Grid (available from https://www.gebco.net/data_and_products/gridded_bathymetry_data/). The W-phase code can be downloaded from http://wphase.unistra.fr/wiki/doku.php/wphase. We obtained earthquake information from the GCMT Catalog (https://www.globalcmt.org/). We plotted focal mechanisms representing moment tensors with a MATLAB code developed by James Conder (available from MATLAB Central File Exchange (https://www.mathworks.com/matlabcentral/fileexchange/61227-focalmech-fm-centerx-centery-diam-varargin). Data of MT solutions obtained in this study and used for Figure 7 is provided in an open access repository, Zenondo (https://doi.org/10.5281/zenodo.4442967).

References

Acocella, V. (2007). Understanding caldera structure and development: An overview of analogue models compared to natural calderas. *Earth-Science Reviews*, *85*(3–4), 125–160. https://doi.org/10.1016/j.earscirev.2007.08.004

Aki, K., & Richards, P. G. (1980). *Quantitative seismology*. Sausalito, CA: University Science Books.

Amelung, F., Jonsson, S., Zebker, H., & Segall, P. (2000). Widespread uplift and "trapdoor" faulting on Galapagos volcanoes observed with radar interferometry. *Nature*, *407*(6807), 993–996. https://doi.org/10.1038/35039604

Anderson, K. R., Johanson, I. A., Patrick, M. R., Gu, M., Segall, P., Poland, M. P., et al. (2019). Magma reservoir failure and the onset of caldera collapse at Kīlauea Volcano in 2018. *Science*, *366*(6470). https://doi.org/10.1126/science.aaz1822

Cesca, S., Letort, J., Razafindrakoto, H. N. T., Heimann, S., Rivalta, E., Isken, M. P., et al. (2020). Drainage of a deep magma reservoir near Mayotte inferred from seismicity and deformation. *Nature Geoscience*, *13*(1), 87–93. https://doi.org/10.1038/s41561-019-0505-5

Chadwick, W. W., Geist, D. J., Jónsson, S., Poland, M., Johnson, D. J., & Meertens, C. M. (2006). A volcano bursting at the seams: Inflation, faulting, and eruption at Sierra Negra volcano, Galápagos. *Geology*, *34*(12), 1025–1028. https://doi.org/10.1130/G22826A.1

Chouet, B. (2003). Volcano Seismology. *Pure and Applied Geophysics*, *160*(3), 739–788. https://doi.org/10.1007/PL00012556

Chu, R., Zhu, L., & Helmberger, D. V. (2009). Determination of earthquake focal depths and source time functions in central Asia using teleseismic P waveforms. *Geophysical Research Letters*, *36*(17), 7–10. https://doi.org/10.1029/2009GL039494

Cole, J. W., Milner, D. M., & Spinks, K. D. (2005). Calderas and caldera structures: A review. *Earth-Science Reviews*, *69*(1–2), 1–26. https://doi.org/10.1016/j.earscirev.2004.06.004

Contreras-Arratia, R., & Neuberg, J. W. (2019). Complex seismic sources in volcanic environments: Radiation modelling and moment tensor inversions. *Journal of Volcanology and Geothermal Research*, *381*, 262–272. https://doi.org/10.1016/j.jvolgeores.2019.06.005

Contreras-Arratia, R., & Neuberg, J. W. (2020). Towards reconciling seismic and geodetic moment estimations: Case Bárðarbunga. *Journal of Volcanology and Geothermal Research*, 107034. https://doi.org/10.1016/j.jvolgeores.2020.107034

Dahlen, F. A., & Tromp, J. (1998). *Theoretical global seismology*. *Theoretical global seismology*. https://doi.org/10.1029/99eo00054

Darnet, M., Wawrzyniak, P., Tarits, P., Hautot, S., & D'Eu, J. F. (2020). Mapping the geometry of volcanic systems with magnetotelluric soundings: Results from a land and marine magnetotelluric survey performed during the 2018–2019 Mayotte seismovolcanic crisis.

Journal of Volcanology and Geothermal Research, *406*, 107046. https://doi.org/10.1016/j.jvolgeores.2020.107046

Duputel, Z., & Rivera, L. (2019). The 2007 caldera collapse of Piton de la Fournaise volcano: Source process from very-long-period seismic signals. *Earth and Planetary Science Letters*, *527*, 115786. https://doi.org/10.1016/j.epsl.2019.115786

Duputel, Z., Rivera, L., Kanamori, H., & Hayes, G. (2012). W phase source inversion for moderate to large earthquakes (1990-2010). *Geophysical Journal International*, *189*(2), 1125–1147. https://doi.org/10.1111/j.1365-246X.2012.05419.x

Dziewonski, A. M., Chou, T. A., & Woodhouse, J. H. (1981). Determination of earthquake source parameters from waveform data for studies of global and regional seismicity. *Journal of Geophysical Research*. https://doi.org/10.1029/JB086iB04p02825

Dziewonski, A. M., & Anderson, D. L. (1981). Preliminary reference Earth model. *Physics of the Earth and Planetary Interiors*, *25*(4), 297–356. https://doi.org/10.1016/0031-9201(81)90046-7

Ekström, G., Nettles, M., & Dziewoński, A. M. (2012). The global CMT project 2004-2010: Centroid-moment tensors for 13,017 earthquakes. *Physics of the Earth and Planetary Interiors*, *200–201*, 1–9. https://doi.org/10.1016/j.pepi.2012.04.002

Ekström, G. (1994). Anomalous earthquakes on volcano ring-fault structures. *Earth and Planetary*

Science Letters, *128*(3–4), 707–712. https://doi.org/10.1016/0012-821X(94)90184-8

Fontaine, F. R., Roult, G., Hejrani, B., Michon, L., Ferrazzini, V., Barruol, G., et al. (2019). Very- and ultra-long-period seismic signals prior to and during caldera formation on La Réunion Island. *Scientific Reports*, *9*(1). https://doi.org/10.1038/s41598-019-44439-1

Frohlich, C. (1994). Earthquakes with Non-Double-Couple Mechanisms. *Science*, *264*(5160), 804–809. https://doi.org/10.1126/science.264.5160.804

Fukao, Y., Sandanbata, O., Sugioka, H., Ito, A., Shiobara, H., Watada, S., & Satake, K. (2018). Mechanism of the 2015 volcanic tsunami earthquake near Torishima, Japan. *Science Advances*, *4*(4). https://doi.org/10.1126/sciadv.aao0219

Geist, D. J., Harpp, K. S., Naumann, T. R., Poland, M., Chadwick, W. W., Hall, M., & Rader, E. (2008). The 2005 eruption of Sierra Negra volcano, Galápagos, Ecuador. *Bulletin of Volcanology*, *70*(6), 655–673. https://doi.org/10.1007/s00445-007-0160-3

Geyer, A., & Martí, J. (2014). A short review of our current understanding of the development of ring faults during collapse caldera formation. *Frontiers in Earth Science*, *2*(September), 1–13. https://doi.org/10.3389/feart.2014.00022

Gilbert, F. (1971). Excitation of the Normal Modes of the Earth by Earthquake Sources. *Geophysical Journal of the Royal Astronomical Society*, *22*(2), 223–226. https://doi.org/10.1111/j.1365-246X.1971.tb03593.x

Global Volcanism Program. (2005). Report on Sierra Negra (Ecuador). *Bulletin of the Global Volcanism Network*, *30*(9). https://doi.org/10.5479/si.GVP.BGVN200509-353050

Global Volcanism Program. (2018). Report on Sierra Negra (Ecuador). *Bulletin of the Global Volcanism Network*, *43*(9). https://doi.org/10.5479/si.GVP.BGVN201809-353050

Gudmundsson, M. T., Jónsdóttir, K., Hooper, A., Holohan, E. P., Halldórsson, S. A., Ófeigsson, B. G., et al. (2016). Gradual caldera collapse at Bárdarbunga volcano, Iceland, regulated by lateral magma outflow. *Science*, *353*(6296). https://doi.org/10.1126/science.aaf8988

Gusman, A. R., Kaneko, Y., Power, W., & Burbidge, D. (2020). Source model for two enigmatic repeating vertical-T CLVD tsunami earthquakes in the Kermadec Ridge. *Geophysical Research Letters*, *47*(16). https://doi.org/10.1029/2020gl087805

Hanks, T. C., & Kanamori, H. (1979). A moment magnitude scale. In *Journal of Geophysical Research B: Solid Earth*. https://doi.org/10.1029/JB084iB05p02348

Hayes, G. P., Rivera, L., & Kanamori, H. (2009). Source inversion of the W-phase: Realtime implementation and extension to low magnitudes. *Seismological Research Letters*, *80*(5), 817–822. https://doi.org/10.1785/gssrl.80.5.817

Hejrani, B., & Tkalčić, H. (2020). Resolvability of the centroid-moment-tensors for shallow seismic sources and improvements from modelling high-frequency waveforms. *Journal of Geophysical Research: Solid Earth*, (February 2019), 1–13.

https://doi.org/10.1029/2020JB019643

Jónsson, S. (2009). Stress interaction between magma accumulation and trapdoor faulting on Sierra Negra volcano, Galápagos. *Tectonophysics*, *471*(1–2), 36–44. https://doi.org/10.1016/j.tecto.2008.08.005

Kanamori, H., Given, J. W., & Lay, T. (1984). Analysis of seismic body waves excited by the Mount St. Helens eruption of May 18, 1980. *Journal of Geophysical Research: Solid Earth*, *89*(B3), 1856–1866. https://doi.org/10.1029/JB089iB03p01856

Kanamori, H. (1977). The energy release in great earthquakes. *Journal of Geophysical Research*. https://doi.org/10.1029/jb082i020p02981

Kanamori, H., Ekström, G., Dziewonski, A., Barker, J. S., & Sipkin, S. A. (1993). Seismic radiation by magma injection: An anomalous seismic event near Tori Shima, Japan. *Journal of Geophysical Research: Solid Earth*, *98*(B4), 6511–6522. https://doi.org/10.1029/92JB02867

Kanamori, H., & Given, J. W. (1982). Analysis of long-period seismic waves excited by the May 18, 1980, eruption of Mount St. Helens-A terrestrial monopole? *Journal of Geophysical Research: Solid Earth*, *87*(B7), 5422–5432. https://doi.org/10.1029/JB087iB07p05422

Kanamori, H., & Given, J. W. (1981). Use of long-period surface waves for rapid determination of earthquake-source parameters. *Physics of the Earth and Planetary Interiors*, *27*(1), 8–31. https://doi.org/10.1016/0031-9201(81)90083-2

Kanamori, H., & Mori, J. (1992). Harmonic excitation of mantle Rayleigh waves by the 1991 eruption of Mount Pinatubo, Philippines. *Geophysical Research Letters*, *19*(7), 721–724. https://doi.org/10.1029/92GL00258

Kanamori, H., & Rivera, L. (2008). Source inversion of W phase: Speeding up seismic tsunami warning. *Geophysical Journal International*, *175*(1), 222–238. https://doi.org/10.1111/j.1365-246X.2008.03887.x

Kawakatsu, H., & Yamamoto, M. (2015). *Volcano Seismology*. *Treatise on Geophysics: Second Edition* (Vol. 4). Elsevier B.V. https://doi.org/10.1016/B978-0-444-53802-4.00081-6

Kawakatsu, H. (1996). Observability of the isotropic component of a moment tensor. *Geophysical Journal International*, *126*(2), 525–544. https://doi.org/10.1111/j.1365-246X.1996.tb05308.x

La Femina, P. C., Ruiz Paspuel, A. G., Higgins, M., Geirsson, H., Geist, D., & Mothes, P. A. (2018). The June 26, 2018 Eruption of Sierra Negra Volcano, Galapagos Islands, Ecuador: Pre-, Co-and Post-Eruptive Deformation from GPS Geodesy. *AGUFM 2018*, V31C-08. Retrieved from https://ui.adsabs.harvard.edu/abs/2018AGUFM.V31C..08L

McKee, C. O., Lowenstein, P. L., De Saint Ours, P., Talai, B., Itikarai, I., & Mori, J. J. (1984). Seismic and ground deformation crises at Rabaul Caldera: Prelude to an eruption? *Bulletin Volcanologique*, *47*(2), 397–411. https://doi.org/10.1007/BF01961569

McNutt, S. R. (2002). 25 Volcano seismology and monitoring for eruptions. *International*

Geophysics, *81*(A), 383–406. https://doi.org/10.1016/S0074-6142(02)80228-5

Mori, J., & McKee, C. (1987). Outward-dipping ring- fault structure at Rabaul Caldera as shown by earthquake locations (Papua New Guinea). *Science*, *235*(4785), 193–195. https://doi.org/10.1126/science.235.4785.193

Mori, J., McKee, C., Itikarai, I., Lowenstein, P., de Saint Ours, P., & Talai, B. (1989). Earthquakes of the Rabaul Seismo-Deformational Crisis September 1983 to July 1985: Seismicity on a Caldera Ring Fault (pp. 429–462). Springer, Berlin, Heidelberg. https://doi.org/10.1007/978-3-642-73759-6_25

Neal, C. A., Brantley, S. R., Antolik, L., Babb, J. L., Burgess, M., Calles, K., et al. (2019). The 2018 rift eruption and summit collapse of Kīlauea Volcano. *Science*, *363*(6425), 367–374. https://doi.org/10.1126/science.aav7046

Nettles, M., & Ekström, G. (1998). Faulting mechanism of anomalous earthquakes near Bárdarbunga Volcano, Iceland. *Journal of Geophysical Research: Solid Earth*, *103*(8), 17973–17983. https://doi.org/10.1029/98jb01392

Parks, M. M., Heimisson, E. R., Sigmundsson, F., Hooper, A., Vogfjörd, K. S., Árnadóttir, T., et al. (2017). Evolution of deformation and stress changes during the caldera collapse and dyking at Bárdarbunga, 2014–2015: Implication for triggering of seismicity at nearby Tungnafellsjökull volcano. *Earth and Planetary Science Letters*, *462*, 212–223. https://doi.org/10.1016/j.epsl.2017.01.020

Reynolds, R. W., Geist, D., & Kurz, M. D. (1995). Physical volcanology and structural development of Sierra Negra volcano, Isabela Island, Galapagos archipelago. *Geological Society of America Bulletin*, *107*(12), 1398–1410. https://doi.org/10.1130/0016-7606(1995)107<1398:PVASDO>2.3.CO;2

Riel, B., Milillo, P., Simons, M., Lundgren, P., Kanamori, H., & Samsonov, S. (2015). The collapse of BárÐarbunga caldera, Iceland. *Geophysical Journal International*, *202*(1), 446–453. https://doi.org/10.1093/gji/ggv157

Sandanbata, O., Watada, S., Satake, K., Fukao, Y., Sugioka, H., Ito, A., & Shiobara, H. (2018). Ray Tracing for Dispersive Tsunamis and Source Amplitude Estimation Based on Green's Law: Application to the 2015 Volcanic Tsunami Earthquake Near Torishima, South of Japan. *Pure and Applied Geophysics*, *175*(4), 1371–1385. https://doi.org/10.1007/s00024-017-1746-0

Satake, K., & Kanamori, H. (1991). Abnormal tsunamis caused by the June 13, 1984, Torishima, Japan, earthquake. *Journal of Geophysical Research*, *96*(B12), 933–939. https://doi.org/10.1029/91jb01903

Segall, P., Anderson, K. R., Johanson, I., & Miklius, A. (2019). Mechanics of Inflationary Deformation During Caldera Collapse: Evidence From the 2018 Kīlauea Eruption. *Geophysical Research Letters*, *46*(21), 11782–11789. https://doi.org/10.1029/2019GL084689

Segall, P., Anderson, K. R., Pulvirenti, F., Wang, T., & Johanson, I. (2020). Caldera collapse geometry revealed by near-field GPS displacements at Kīlauea Volcano in 2018. *Geophsical*

Research Letters, 1–17. https://doi.org/10.1029/2020GL088867

Shearer, P. M. (2009). *Introduction to Seismology*. *Geophysical Journal of the Royal Astronomical Society* (Vol. 40). Cambridge: Cambridge University Press. https://doi.org/10.1017/CBO9780511841552

Shuler, A., & Ekström, G. (2009). Anomalous earthquakes associated with Nyiragongo Volcano: Observations and potential mechanisms. *Journal of Volcanology and Geothermal Research*, *181*(3–4), 219–230. https://doi.org/10.1016/j.jvolgeores.2009.01.011

Shuler, A., Nettles, M., & Ekström, G. (2013a). Global observation of vertical-CLVD earthquakes at active volcanoes. *Journal of Geophysical Research: Solid Earth*, *118*(1), 138–164. https://doi.org/10.1029/2012JB009721

Shuler, A., Ekström, G., & Nettles, M. (2013b). Physical mechanisms for vertical-CLVD earthquakes at active volcanoes. *Journal of Geophysical Research: Solid Earth*, *118*(4), 1569–1586. https://doi.org/10.1002/jgrb.50131

Silver, P. G., & Jordan, T. H. (1982). Optimal estimation of scalar seismic moment. *Geophysical Journal of the Royal Astronomical Society*, *70*(3), 755–787. https://doi.org/10.1111/j.1365-246X.1982.tb05982.x

Tadono, T., Ishida, H., Oda, F., Naito, S., Minakawa, K., & Iwamoto, H. (2014). Precise Global DEM Generation by ALOS PRISM. *ISPRS Annals of Photogrammetry, Remote Sensing and Spatial*

Information Sciences, *II–4*(May), 71–76. https://doi.org/10.5194/isprsannals-ii-4-71-2014

Takeuchi, H., & Saito, M. (1972). Seismic Surface Waves. In *Methods in Computational Physics: Advances in Research and Applications* (Vol. 11, pp. 217–295). https://doi.org/10.1016/B978-0-12-460811-5.50010-6

Tepp, G., Hotovec-Ellis, A., Shiro, B., Johanson, I., Thelen, W., & Haney, M. M. (2020). Seismic and geodetic progression of the 2018 summit caldera collapse of Kīlauea volcano. *Earth and Planetary Science Letters*, *540*, 116250. https://doi.org/10.1016/j.epsl.2020.116250

Vasconez, F., Ramón, P., Hernandez, S., Hidalgo, S., Bernard, B., Ruiz, M., et al. (2018). The different characteristics of the recent eruptions of Fernandina and Sierra Negra volcanoes (Galápagos, Ecuador). *Volcanica*, *1*(2), 127–133. https://doi.org/10.30909/vol.01.02.127133

Wimpenny, S., & Watson, C. S. (2020). gWFM: A Global Catalog of Moderate-Magnitude Earthquakes Studied Using Teleseismic Body Waves. *Seismological Research Letters*. https://doi.org/10.1785/0220200218

Yun, S., Segall, P., & Zebker, H. (2006). Constraints on magma chamber geometry at Sierra Negra Volcano, Galápagos Islands, based on InSAR observations. *Journal of Volcanology and Geothermal Research*, *150*(1–3), 232–243. https://doi.org/10.1016/j.jvolgeores.2005.07.009

Yun, S.-H. (2007). A mechanical model of the large-deformation 2005 Sierra Negra volcanic eruption derived from InSAR measurements. *PhD Thesis, Department of Geophysics, Stanford*

University.

Figures and tables

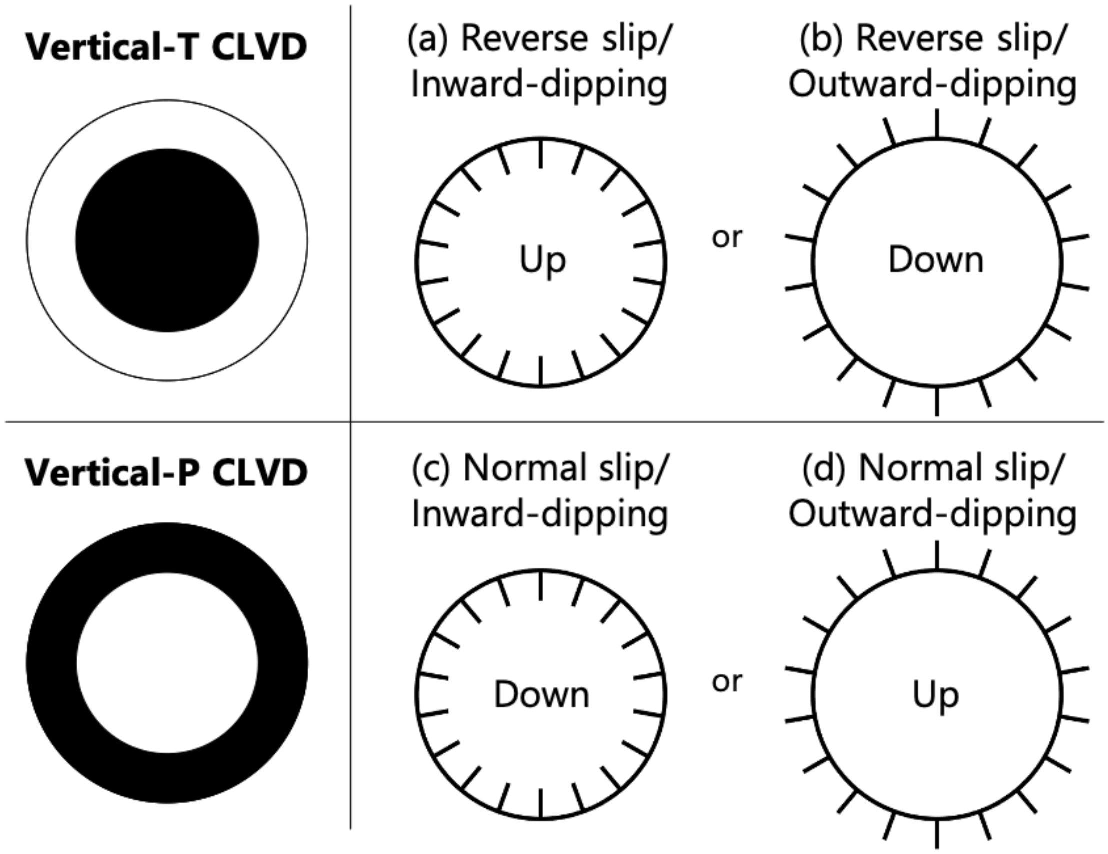

Figure 1 Two types of vertical-CLVD earthquake caused by ring-faulting.

(a–d) The kinematics and geometry of ring-faulting corresponding to the two endmembers of vertical-CLVD earthquakes (shown on the left). The circle represents the up-dip end of the ring fault, with short lines indicating the dip direction to the down-dip end. The direction of motion of the central block is indicated at the center of the circle.

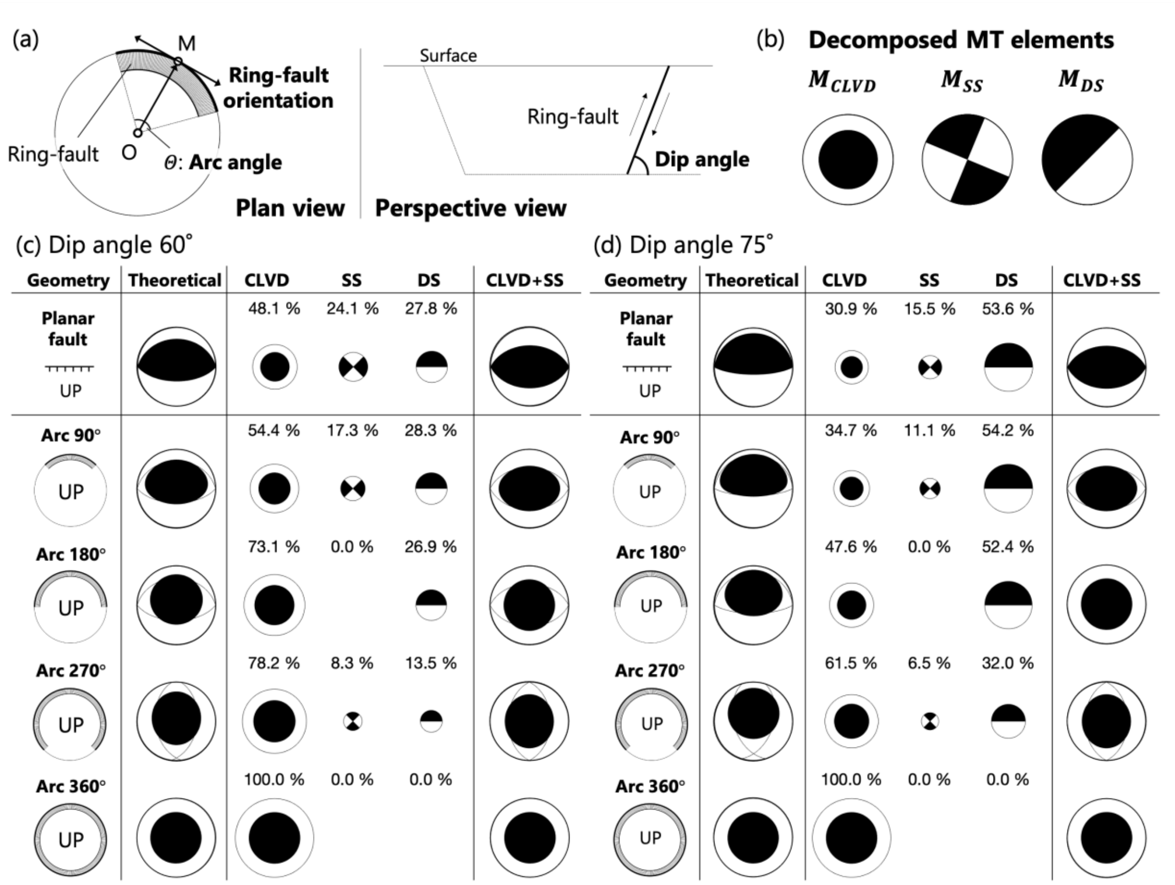

Figure 2 Modeling and decomposition of theoretical moment tensors of idealized ring-faulting. (a) Ring-fault parameters. Thick and thin arc curves represent up-dip and down-dip ends, respectively. The ring fault is discretized by rhomboidal planar faults with an arc angle of 1°, each of which has a reverse slip of 1 m. Arc and dip angles and the *ring-fault azimuth* ($\overrightarrow{OM}$) are variable parameters. The *ring-fault orientation* is perpendicular to the ring-fault azimuth. The *dip angle* is uniform along the ring fault. (b) Three decomposed moment tensor (MT) components. (c–d) Theoretical MTs of ring-faulting with arc angles of 90°, 180°, 270°, and 360° and with dip angles of (c) 60° and (d) 75°. Columns: (1) kinematics and geometry of ring-faulting, (2–6) focal mechanism diagrams of the theoretical MT (2), decomposed MT components (*CLVD*, *SS*, and *DS*) with their ratios (3–5), and resolvable MTs (6). The orientation of the *best double-couple solution*

is shown by thin curves in columns 2 and 6. All focal mechanisms are shown by projection of the lower focal hemisphere. The diameter of the focal mechanism diagram is proportional to its scalar moment but slightly exaggerated for the component with percentages of <10% for clear visualization. Thin curves on the diagram represent the nodal planes of the best-fitting double-couple moment tensor (see text in Section 2.2).

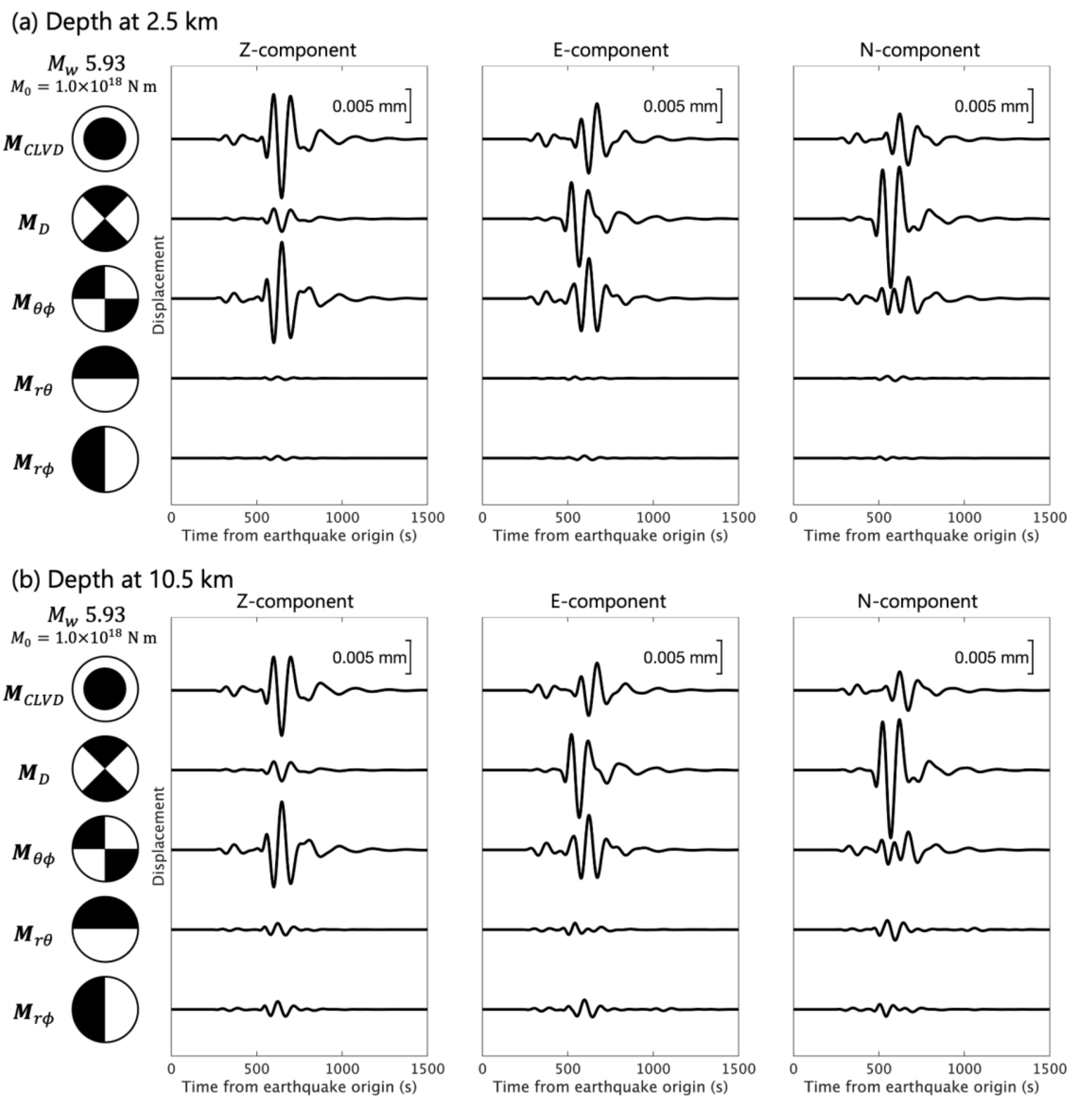

Figure 3 Synthetic long-period seismic waves from five components of a moment tensor.

Synthetic long-period seismic waveforms from sources representing five components of a moment tensor. The centroid depth is (a) 2.5 km and (b) 10.5 km below the solid surface. $\boldsymbol{M}_D$ and $\boldsymbol{M}_{\theta\phi}$ determine the *SS* component, and $\boldsymbol{M}_{r\theta}$ and $\boldsymbol{M}_{r\phi}$ determine the *DS* component. The virtual station is located at (φ, Δ) = (19.2°, 17.8°), where φ is the station azimuth from north (eastward positive), and Δ is the distance from the source. We used the W-phase code (Kanamori and Rivera, 2008; Hayes et al., 2009; Duputel et al., 2012) for the convolution of Green's functions and filtering. Green's functions are computed by the normal mode method (e.g., Takeuchi and Saito, 1972), with the 1-D Preliminary Reference Earth Model (PREM; Dziewonski and Anderson, 1981). A one-pass and fourth-order Butterworth Bandpass filter with corner frequencies of 0.005 and 0.0125 Hz was applied.

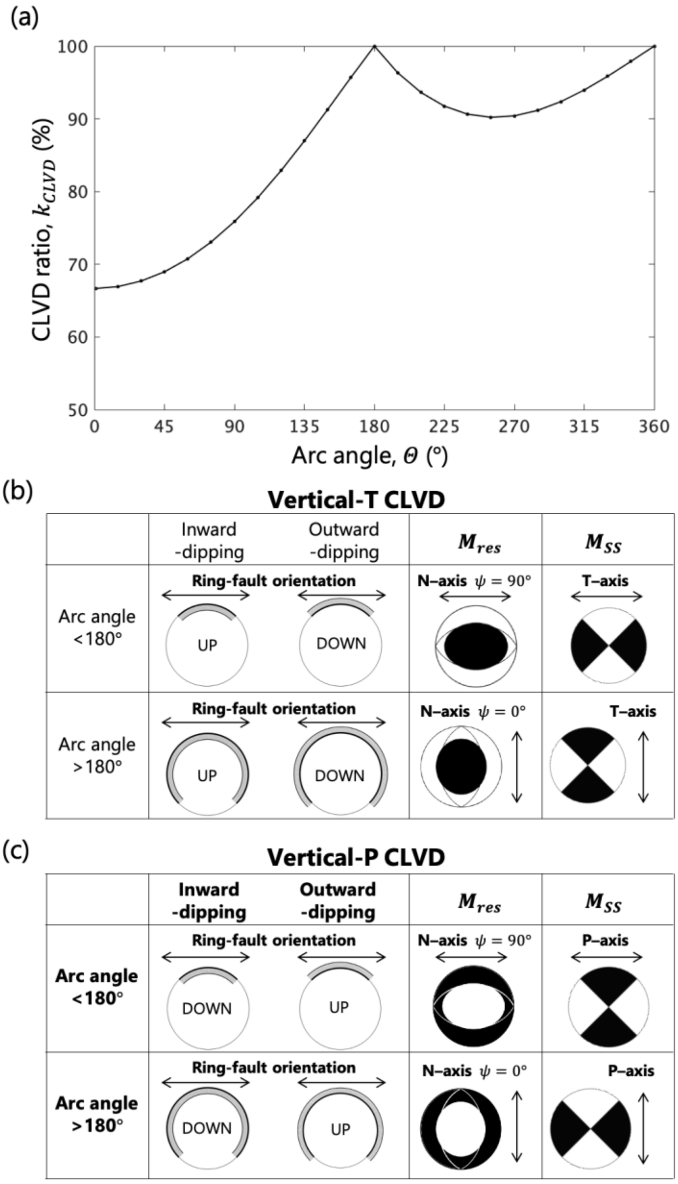

Figure 4 Relationship between M_{res} and fault parameters of ring-faulting.

(a) The CLVD ratio, k_{CLVD}, in the resolvable MT, $\boldsymbol{M}_{res}$, as a function of arc angle Θ. Note that the relationship between k_{CLVD} and Θ is independent of the dip angle of the ring fault. (b–c) Relationship between ring-fault geometry and $\boldsymbol{M}_{res}$ for (b) vertical-T earthquakes and (c) vertical-P earthquakes. In the 2nd column, the dip direction of the ring fault (inward or outward), the kinematics of the central block (up or down), and the ring-fault orientation (an arrow) are also shown. In the 3rd column, $\boldsymbol{M}_{res}$ is shown with the orientation of its *N-axis* (arrow). In the 4th column, the *SS* component is shown with its T- or P-axis (arrow). Note that the N-axis of $\boldsymbol{M}_{res}$ is the same as the T- and P-axes of the *SS* component for vertical-T and vertical-P earthquakes, respectively.

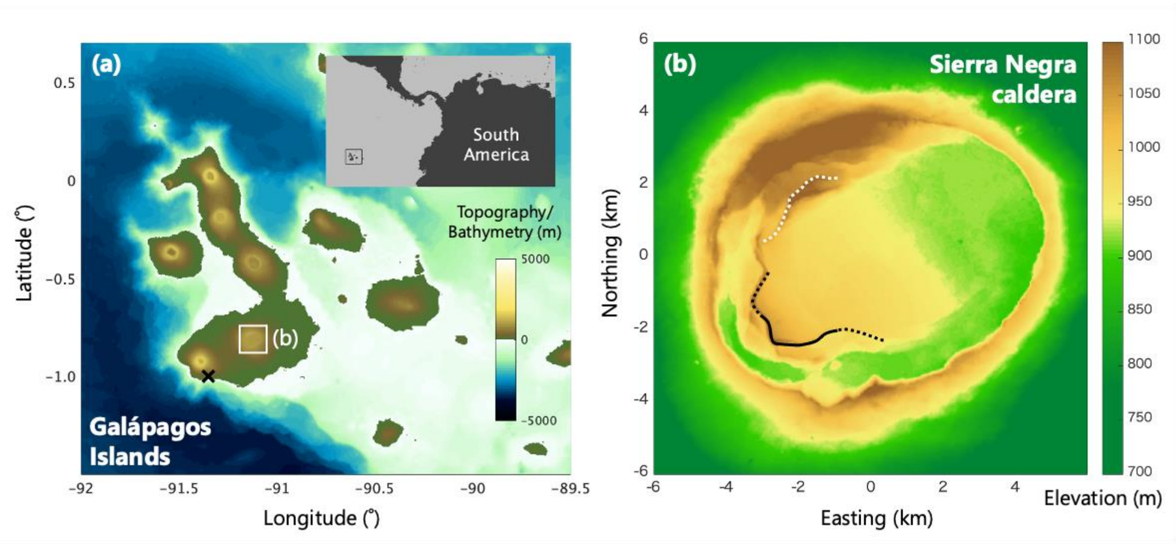

Figure 5 Maps of the Galápagos Islands and the Sierra Negra caldera.

(a) Map of the Galápagos Islands. Topographic and bathymetric data were downloaded from GEBCO 2019. The black rectangle in the inset panel indicates the area shown in (a). The black cross represents the centroid location of the vertical-T earthquake of 22 October 2005 reported in the GCMT Catalog. (b) Map of the Sierra Negra caldera. Topographic data were downloaded from the Advance Land Observation Satellite (ALOS) World 3D–30 m DEM (AW3D30) provided by the Japan Aerospace Exploration Agency (JAXA) (e.g., Tadono et al., 2014). The black curve indicates the fresh vertical scarp identified by Geist et al. (2008) during a field survey in June 2006. The part represented by the solid curve was clearly identified, whereas those along the dotted curves were less clearly defined. The dotted white curve indicates a possible geometry inferred in this study for the 2018 vertical-P earthquake (see text in Section 3.4).

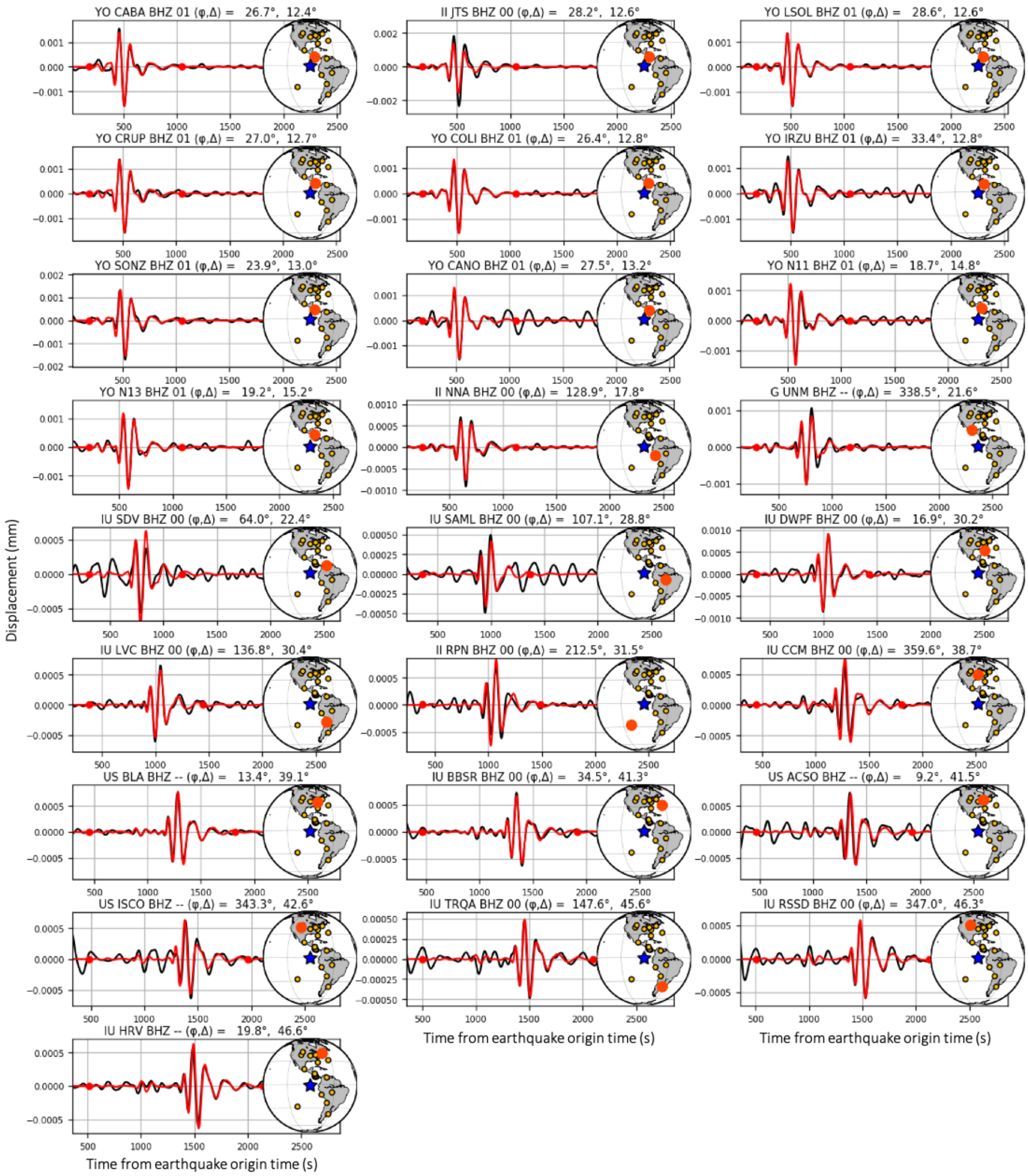

Figure 6 Model performance of MT inversion for the M_w 5.5 vertical-T CLVD earthquake of 22 October 2005.

Red and black lines represent synthetic and observed waveforms, respectively. The start and end points of the inversion time window are indicated by red circles. In each inset map, the blue star and large red circle represent locations of the epicenter (0.83°S, 91.14°W) and the station. The station azimuth (φ) and epicentral distance (Δ) are indicated at the top of each panel.

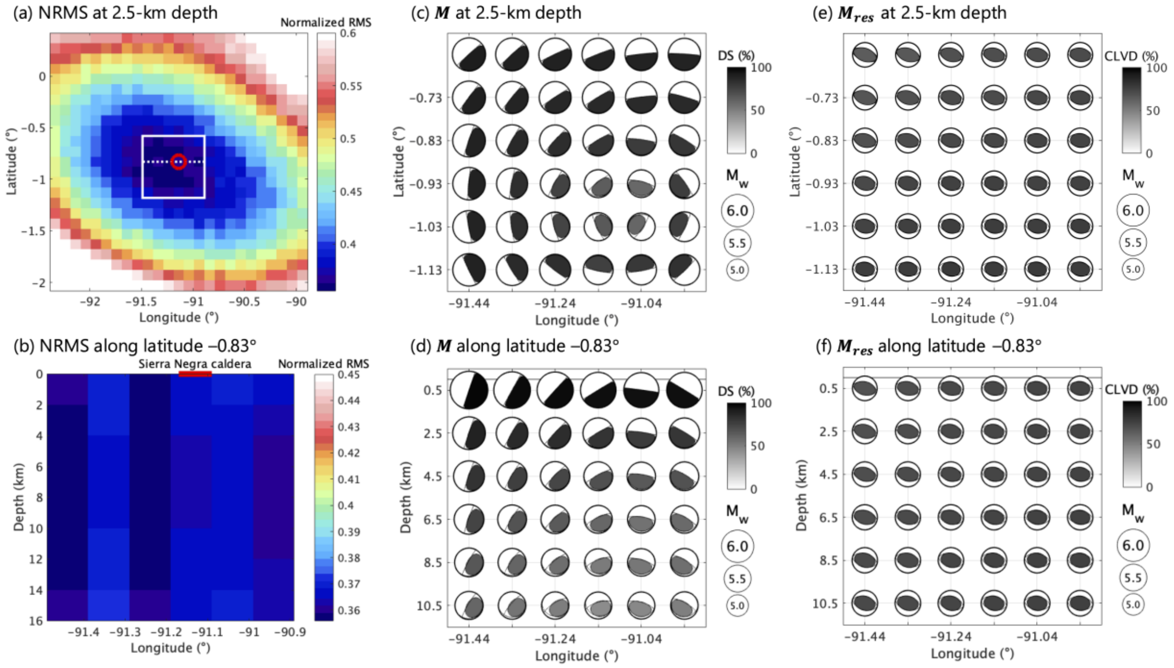

Figure 7 MT inversion for the vertical-T CLVD earthquake of 22 October 2005 at the Sierra Negra caldera.

(a–b) NRMS misfits of MT solutions at source locations distributed on (a) the x–y plane at a depth of 2.5 km and (b) the x–z plane along a latitude of 0.83° (dashed white line in (a)). The red circle in (a) and the red line in (b) represent the approximate locations of the Sierra Negra caldera. (c) MT solutions at different centroid locations on (c) the x–y plane at a depth of 2.5 km in the area shown by the white rectangle in (a) and (d) the x–z plane along a latitude of 0.83°. (e–f) Resolvable MTs on (e) the x–y plane and (f) the x–z plane. All focal mechanisms are shown by projection of the lower focal hemisphere.

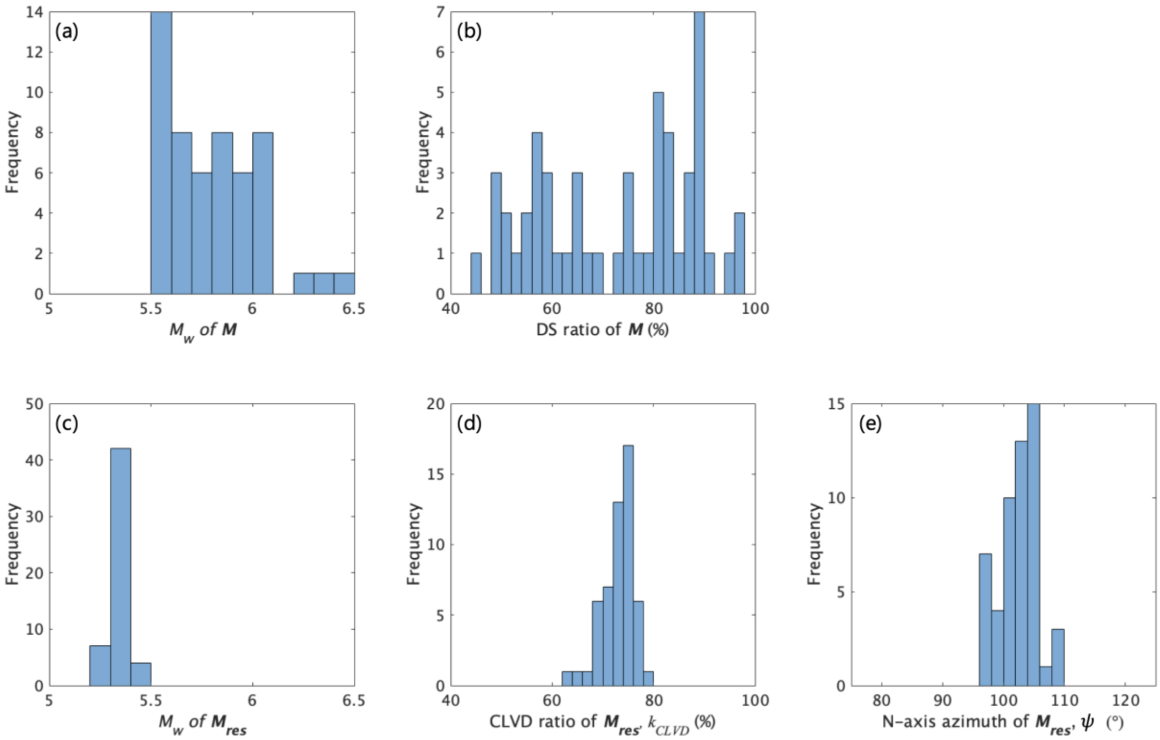

Figure 8 Histogram of the parameters of acceptable MT solutions.

(a) M_w and (b) the ratio of the *DS* component of acceptable MT solutions. (c) M_w, (d) the CLVD ratio k_{CLVD}, and (e) the N-axis azimuth ψ of $\boldsymbol{M}_{res}$ extracted from acceptable MT solutions.

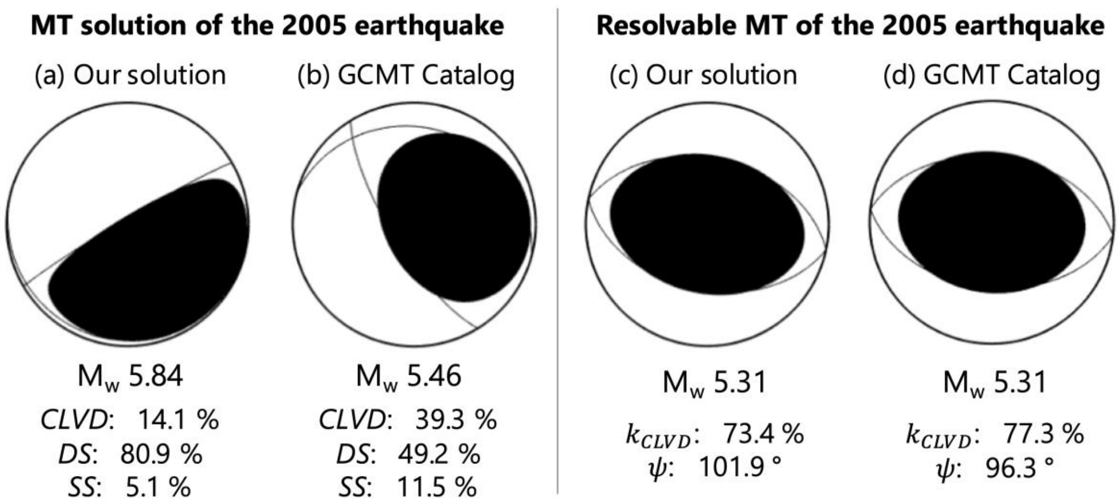

Figure 9 MT solutions and resolvable MTs of the M_w 5.5 vertical-T CLVD earthquake of 22 October 2005.

(a) MT solution with the ratios of components and (c) resolvable MT with the ratio of the *CLVD* component k_{CLVD} to the N-axis azimuth ψ obtained from our MT inversion at a depth of 2.5 km just below the caldera. (b) MT and (d) resolvable MT obtained from the GCMT Catalog. All focal mechanisms are shown by projection of the lower focal hemisphere.

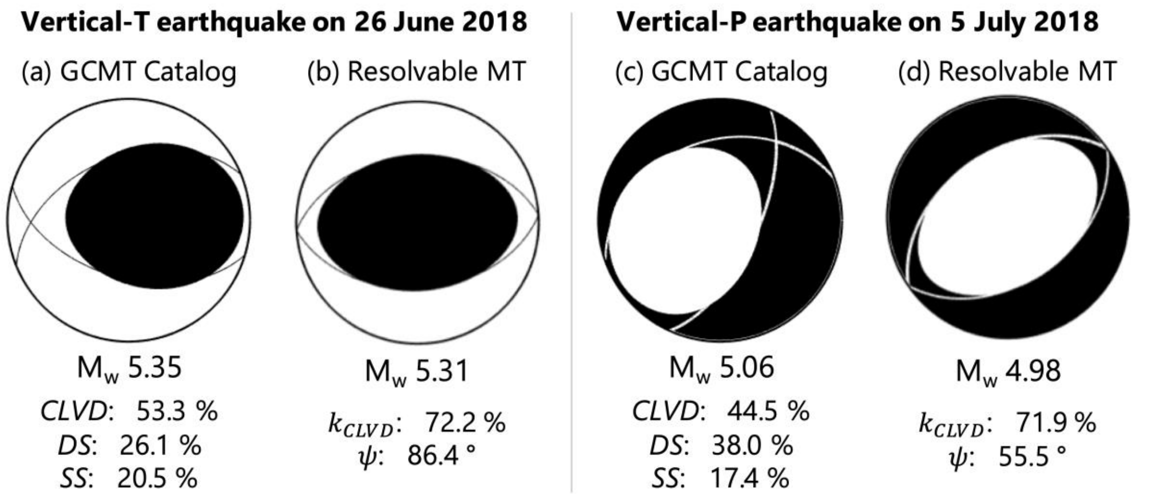

Figure 10 GCMT solutions for two vertical-CLVD earthquakes during the 2018 volcanic activity.

(a) MT solution with the ratios of components and (b) resolvable MT of the M_w 5.3 earthquake of 26 June 2018 with the ratio of the *CLVD* component k_{CLVD} to the N-axis azimuth ψ obtained from the GCMT Catalog. (c–d) The same as (a–b) but for the M_w 5.1 earthquake of 5 July 2018. All focal mechanisms are shown by projection of the lower focal hemisphere.

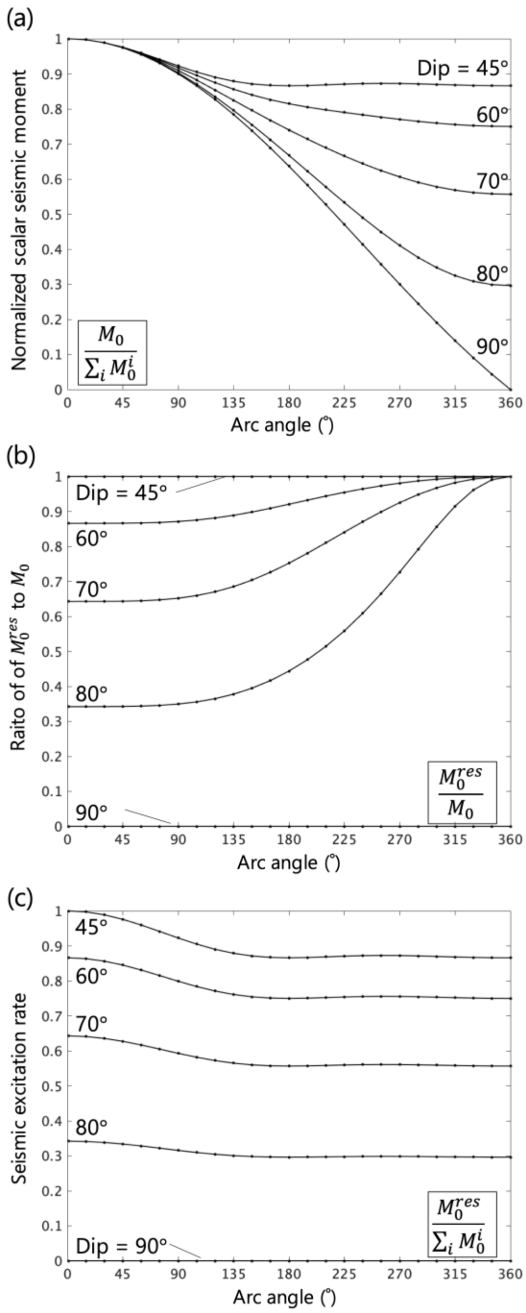

Figure 11 Seismic excitation rate of ring-faulting at a shallow source depth.

(a) Geometrical cancellation of the scalar moment of idealized ring-faulting, calculated using Equation (13). (b) The ratio of M_0^{res} to M_0 of idealized ring-faulting, calculated using Equation (14). (c) The combined effect of (a) and (b), calculated using Equation (15).

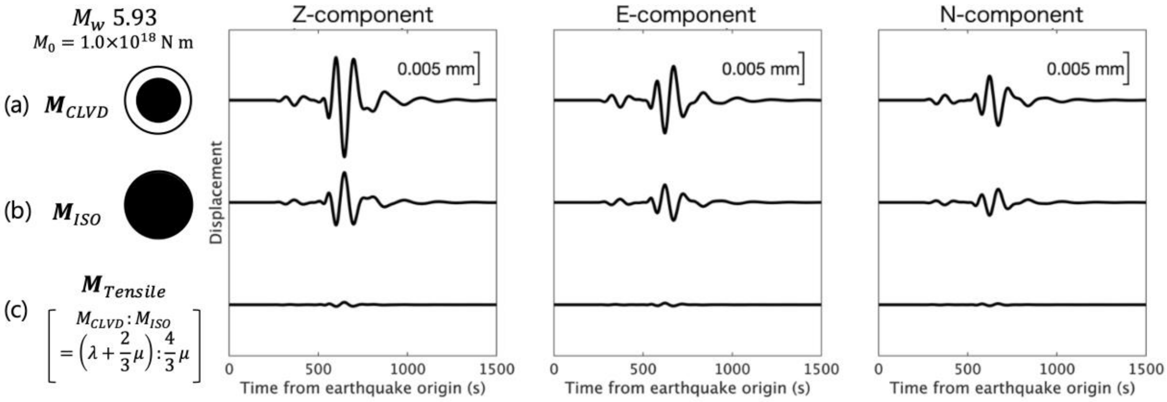

Figure 12 Effects of an isotropic source on estimation of the CLVD source.

Synthetic long-period seismic waveforms of (a) a CLVD source (Equation 25), (b) an isotropic source (Equation 26), and (c) a horizontal tensile source (Equation 27). The MT of the horizontal tensile crack consists of *CLVD* and *ISO* components with a ratio of $M_{ISO}: M_{CLVD} = \left(\lambda + \frac{2}{3}\mu\right) : \frac{4}{3}\mu$, as given in Equation (17). The centroid depth is assumed to be 2.5 km below the solid surface. The station location and filtering procedure are the same as those used for Figure 3.

Event date	Source of solution	Longitude (°W)	Latitude (°S)	Depth (km)	Elements of moment tensor (dyne cm)							M_w
					M_{rr}	$M_{\theta\theta}$	$M_{\phi\phi}$	$M_{r\theta}$	$M_{r\phi}$	$M_{\theta\phi}$	Scale factor (10^{exp})	
22 October 2005	This study	91.14	0.83	2.5	1.246	-1.035	-0.210	-6.127	-3.718	0.182	24	5.84
22 October 2005	GCMT	91.35	1.00	12.0	1.260	-0.989	-0.268	0.459	-1.510	0.080	24	5.46
26 June 2018	GCMT	91.33	0.96	12.0	1.230	-1.090	-0.148	0.118	-0.592	-0.059	24	5.35
5 July 2018	GCMT	90.98	0.88	12.0	-3.880	2.490	1.400	0.314	-3.300	1.420	23	5.06

Table 1 Moment tensor solutions of vertical-CLVD earthquakes for the Sierra Negra caldera.

Centroids and moment tensor solutions of vertical-CLVD earthquakes for the Sierra Negra caldera obtained by MT inversion in this study or taken from the GCMT Catalog. Note that the centroid depth of the GCMT Catalog may be determined at a greater depth (12 km) than the accrual centroid depth of the earthquakes to maintain the stability of the solutions (Ekström et al., 2012).